Robotica (2026), 1–29
doi:10.1017/S0263574726104056

RESEARCH ARTICLE

Dual-loop control of lower-limb exoskeletons using adaptive admittance and nonlinear extended state observer-based active disturbance rejection

Di Zhang, Liuyi Ling and Yiming Liu

Anhui University of Science and Technology, China
Corresponding author: Liuyi Ling; Email: lyling@aust.edu.cn

Received: 7 March 2026 UTC; **Revised:** 9 August 2026 UTC; **Accepted:** 29 September 2026 UTC

Keywords: lower limb exoskeleton; human-robot interaction; adaptive admittance control; nonlinear extended state observer; active disturbance rejection control

Abstract

Lower-limb exoskeleton systems are characterized by strong human–robot coupling, dynamic uncertainties, and multiple concurrent disturbances, which challenge traditional control methods to simultaneously ensure system stability, precise trajectory tracking, and human–robot interaction compliance. To address these challenges, this paper proposes a dual-loop control method tailored for diverse gait rhythms. This method consists of an outer-loop double-layer adaptive admittance control and an inner-loop nonlinear extended state observer-based active disturbance rejection control (NLESO-ADRC). The outer loop establishes baseline admittance parameters based on different velocity levels and performs online adjustments of virtual damping and stiffness by incorporating real-time human–robot interaction torques and admittance corrections, thereby generating smoother and more compliant reference trajectories. The inner loop treats unmodeled dynamics, parameter uncertainties, and friction errors as total system disturbances, which are estimated and compensated for in real-time by the NLESO, thus enhancing joint trajectory-tracking precision and disturbance rejection capabilities. To validate the effectiveness of the proposed approach, various control combinations were constructed based on gait experiment data, and comparative analyses were conducted from multiple perspectives. The results demonstrate that the proposed method not only maintains high trajectory-tracking accuracy and disturbance rejection capabilities across different walking speeds but also achieves compliant regulation during human–robot interaction.

1. Introduction

In recent years, wearable exoskeletons have garnered significant attention from researchers in the medical field [1]. Among these, lower-limb rehabilitation exoskeleton robots represent one of the most typical wearable motion-assistive devices. They provide repetitive and standardized rehabilitation training for patients suffering from stroke, spinal cord injuries, and lower-limb joint disorders. By alleviating the physical burden on therapists while simultaneously enhancing training efficiency and recovery outcomes, they have become a prominent research focal point [2, 3]. Unlike traditional industrial robots, lower-limb exoskeletons are directly coupled with the human body, forming a typical human–robot coupled system [4]. Consequently, achieving safe and comfortable human–robot collaborative control while ensuring motion precision remains a critical challenge in the field of exoskeleton control [5].

Admittance control has been widely applied in exoskeleton control due to its ability to recognize human movement intentions based on the characteristics of human–robot physical interaction, adjust desired motion trajectories, and enhance system compliance and coordination [6, 7] Specifically, the mechanism of admittance control involves an outer loop that reshapes the reference trajectory in real-time based on the captured force/torque information during interaction, which is then executed by an inner-loop tracking controller [8].

© The Author(s), 2026. Published by Cambridge University Press.

Downloaded from https://www.cambridge.org/core. UNIVERSIDAD AUTONOMA METROPOLITANA, on 16 Nov 2026 at 03:23:03, subject to the Cambridge Core terms of use, available at https://www.cambridge.org/core/terms. https://doi.org/10.1017/S0263574726104056

In recent years, researchers have further improved the adaptability of exoskeletons to different human states and interaction conditions through variable admittance and adaptive admittance adjustment. For example, Gao et al. [36] established a human–machine coupling dynamics model for lower-limb rehabilitation robots and used the RMSprop algorithm to adaptively adjust admittance parameters based on human–machine interaction forces, thereby improving human–machine collaborative control performance; Zhan et al. [37] combined dynamic parameter identification with admittance control and used admittance control to coordinate the exoskeleton motion response with human motion intention. The above research indicates that adaptive admittance control can effectively improve the flexibility of human–computer interaction. However, due to the fact that the admittance outer loop essentially changes the robot's motion state by modifying the reference trajectory, its actual control performance still largely depends on the tracking accuracy, robustness, and ability to suppress human–machine coupling disturbances of the inner loop motion controller for time-varying reference trajectories.

Regarding inner-loop control for tracking reference motions generated by admittance control, proportional-integral-derivative (PID) control [9, 10] is widely utilized due to its structural simplicity and ease of implementation. However, it exhibits significant sensitivity to parameter variations and external disturbances, which often compromises control performance in complex human–robot coupling environments. To mitigate the impact of system nonlinearities, researchers have proposed Computed Torque Control (CTC) [11, 12], which incorporates feedforward compensation based on dynamic models. Nevertheless, the efficacy of CTC is highly contingent upon the accuracy of the dynamic model, leaving its robustness susceptible to external disturbances. Consequently, model-based nonlinear control methods – such as Backstepping Control [13, 14], Adaptive Control [15, 16], and Sliding Mode Control (SMC) [17, 18] – have been introduced. Among these, SMC has gained prominence for its inherent robustness against uncertainties. For instance, an adaptive SMC based on the super-twisting algorithm was proposed in ref. [17], although Aole et al. [18] integrated a Linear Extended State Observer with SMC to enhance trajectory-tracking robustness under model uncertainties. Although these advanced SMC variants improve disturbance rejection to some extent, their implementation often remains dependent on actuator models and may introduce undesirable effects such as chattering.

Therefore, there is an urgent need for an inner-loop control method that is less dependent on the system model, capable of real-time estimation and compensation of both internal and external disturbances, and possesses superior robustness to ensure the effective implementation of admittance control. In response to these requirements, active disturbance rejection control (ADRC) offers a compelling approach [19–21]. By constructing an Extended State Observer, ADRC treats system internal uncertainties and external disturbances collectively as a "total disturbance." This total disturbance is estimated and compensated for in real-time, enabling robust control without the necessity of a precise dynamic model [19, 22, 23]. However, the traditional Linear Extended State Observer (LESO) typically relies on high-bandwidth designs to ensure disturbance estimation accuracy. In practical systems, this often amplifies measurement noise and introduces high-frequency chattering, thereby limiting its performance in noise-intensive environments [24]. To address these issues, researchers have explored various improvements in Extended State Observer (ESO) structures and parameter designs. For instance, the introduction of a cascade ESO structure significantly enhances state and disturbance estimation while maintaining system stability, thus improving overall trajectory tracking [25]. Other studies have integrated noise suppression or filtering techniques into the ESO/ADRC framework to bolster robustness against measurement noise [26]. Li et al. [38] further pointed out that ESO is one of the important methods used in robot systems to estimate and compensate for model uncertainty and external disturbances, and is applicable to human–computer interaction robots including exoskeletons.

Building upon these developments, the nonlinear extended state observer (NLESO) has gained increasing attention as a more targeted solution. By incorporating a nonlinear error feedback mechanism, NLESO ensures fast convergence while effectively suppressing noise amplification, demonstrating superior estimation accuracy and robustness in various nonlinear systems [27, 28]. This provides a promising avenue for the inner-loop trajectory-tracking control of lower-limb exoskeletons [29].

It is worth noting that in recent years, researchers have begun to combine admittance regulation with disturbance observation mechanisms to simultaneously improve human–machine interaction flexibility

Downloaded from https://www.cambridge.org/core. UNIVERSIDAD AUTONOMA METROPOLITANA, on 16 Nov 2026 at 03:23:03, subject to the Cambridge Core terms of use, available at https://www.cambridge.org/core/terms. https://doi.org/10.1017/S0263574726104056

and low-level motion control performance. Chen et al. [39] proposed gait prediction and variable admittance control methods for lower-limb exoskeletons and introduced an extended state observer to handle uncertain factors in the system state and interaction process, thereby reducing real-time human–machine interaction torque. Kou et al. [40] further proposed an active passive switching admittance control method combined with a nonlinear disturbance observer, which improves the control performance of lower-limb exoskeletons in different interaction states through a disturbance observation mechanism. In addition, Elstoy and Gwak [41] combined nonlinear disturbance observers, PID sliding mode control, and admittance models to handle disturbances and uncertainties in human–machine coupling dynamics. These studies indicate that codesigning admittance control with disturbance observation or robust inner loop control is an effective technical approach that balances human–machine compliant interaction and trajectory-tracking performance.

Although previous studies have verified the feasibility of combining admittance control with ESO or disturbance observer in improving human–machine interaction compliance and system robustness, there is still room for further research on existing methods. The existing combination control methods mainly focus on the unilateral improvement of admittance parameter adjustment or disturbance observation performance, and the research on the synergistic effect between outer loop compliance adjustment and inner loop trajectory tracking and disturbance suppression under different motion states is still insufficient. In addition, there is still room for further improvement in the disturbance estimation performance of traditional ESO or perturbation observation methods under complex human–machine coupling and measurement noise conditions.

In response to the above issues, this paper proposes a dual loop control method for lower-limb exoskeletons consisting of a double-layer adaptive admittance outer loop and an NLESO-ADRC inner loop. The outer ring adaptively adjusts the admittance parameters based on different motion states and human–computer interaction information to achieve smooth correction of the reference trajectory. The inner loop utilizes NLESO-ADRC to estimate and compensate for the total disturbance of the system in real time, improving the tracking accuracy and anti-interference ability of the corrected reference trajectory, thereby achieving a synergistic improvement of human–machine interaction flexibility, trajectory-tracking accuracy, and system robustness.

The main contributions of this paper are summarized as follows:

1. A dual-loop control framework for lower-limb exoskeletons under different walking speeds is proposed. The framework consists of an outer-loop adaptive admittance controller and an inner-loop NLESO-ADRC controller. The outer loop generates a compliant modified reference trajectory, whereas the inner loop tracks the joint trajectory and estimates and compensates for the lumped disturbance in real time. Therefore, the proposed framework considers trajectory-tracking accuracy, human–exoskeleton interaction compliance, and disturbance rejection capability simultaneously.
2. A dual-layer adaptive admittance regulation mechanism based on walking-speed conditions and interaction states is designed. To address the limitation that traditional admittance control uses fixed parameters and is difficult to adapt to different walking speeds and real-time interaction variations, three treadmill speed conditions, namely 1.2, 2.4, and 3.6 km/h, are used to determine the baseline admittance parameters in the outer layer. In the inner layer, the virtual damping and virtual stiffness are further adjusted online according to the human–exoskeleton interaction torque and admittance modification. In this way, the admittance parameters are updated through a combined strategy of speed-dependent baseline regulation and real-time interaction-state-based adaptive correction, which improves the smoothness and compliance of the reference trajectory modification under different walking-speed conditions.
3. An NLESO-ADRC inner-loop controller based on an NLESO is developed. In this controller, unmodeled dynamics, parameter uncertainties, friction errors, human-exoskeleton interaction disturbances, and control-gain deviations are uniformly treated as lumped disturbances. These disturbances are estimated and compensated for in real time by the NLESO, thereby improving joint trajectory-tracking accuracy and disturbance rejection stability.

Downloaded from https://www.cambridge.org/core. UNIVERSIDAD AUTONOMA METROPOLITANA, on 16 Nov 2026 at 03:23:03, subject to the Cambridge Core terms of use, available at https://www.cambridge.org/core/terms. https://doi.org/10.1017/S0263574726104056

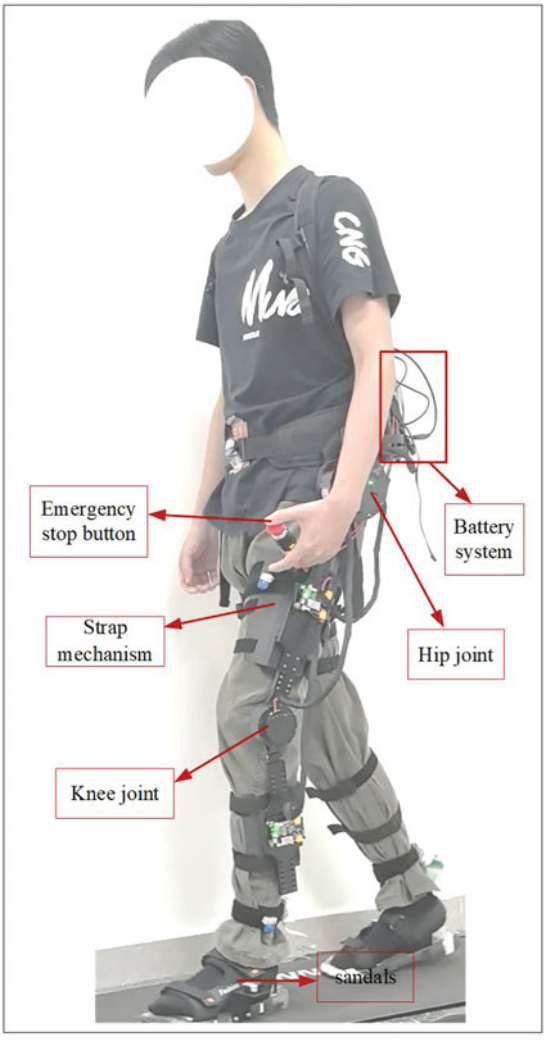


Figure 1. *Lower-limb exoskeleton rehabilitation robot prototype wearing status and main structural components.*

2. Description of the exoskeleton system

This study uses the lower-limb exoskeleton rehabilitation robot prototype shown in Figure 1 as the experimental platform. The exoskeleton mainly consists of a backpack support module, a trunk connection structure, and bilateral lower-limb linkage mechanisms. The total mass of the system is approximately 15.0 kg, excluding the battery. For each lower limb, the hip and knee joints are each equipped with one active flexion/extension degree of freedom in the sagittal plane. The ankle joint has one passive flexion/extension degree of freedom in the sagittal plane and one passive adduction/abduction degree of freedom in the coronal plane. Unless otherwise specified, the joint angles discussed in the following sections refer to flexion/extension motions in the sagittal plane.

To accommodate differences in body size among wearers, the exoskeleton is equipped with an adjustable-width structure in the waist region and length-adjustable mechanisms at the thigh and shank linkages. The adjustment ranges of the thigh and shank linkages are 440–560 and 345–445 mm, respectively. To ensure wearing safety and prevent excessive joint extension, mechanical limit protection

Downloaded from https://www.cambridge.org/core. UNIVERSIDAD AUTONOMA METROPOLITANA, on 16 Nov 2026 at 03:23:03, subject to the Cambridge Core terms of use, available at https://www.cambridge.org/core/terms. https://doi.org/10.1017/S0263574726104056

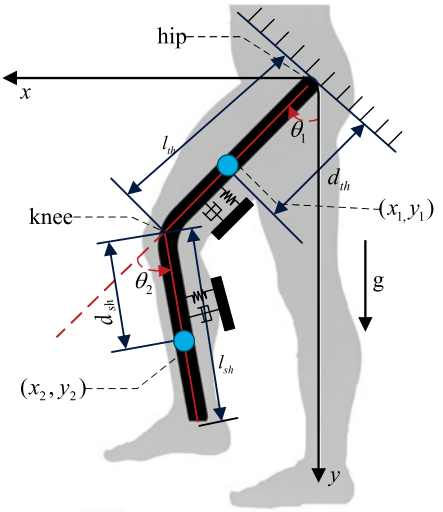


Figure 2. *Two-bar linkage kinematic model of a lower-limb exoskeleton.*

is implemented at each movable joint. The allowable motion ranges of the hip and knee joints are $-0.5236 - 1.0471$ rad and $-1.0471 - 0.1745$ rad, respectively. The entire system is powered by a removable 36 V lithium battery module.

For the actuation system, the hip joint is driven by a DM-J10010L-2EC motor, with rated and peak torques of 40 and 120 N·m, respectively, and is equipped with a 10:1 planetary reducer. The knee joint is driven by a DM-J6006-2EC motor, with rated and peak torques of 4 and 11 N·m, respectively, and is equipped with a 6:1 planetary reducer. Joint state feedback is provided by a motor-side incremental encoder and an output-side absolute position encoder, which are used to obtain joint angle and angular velocity information. The real-time control system is built on an NVIDIA Jetson platform. ROS 2 is used to organize the system data flow, and SocketCAN is employed for motor state reading, Mixed Integrated Torque (MIT) control command transmission, and force sensor data acquisition. The communication frequency of the motors and force sensors is set to 500 Hz, providing a real-time hardware basis for subsequent joint trajectory tracking, interaction force sensing, and admittance control.

3. Dynamic analysis of human–machine coupling models

The primary distinction between lower-limb exoskeleton robots and traditional robots lies in the high degree of coupling between the human body and the exoskeleton, specifically the human–machine interaction [30]. Currently, most analyses of lower-limb exoskeleton dynamics either focus solely on the exoskeleton's own dynamics or model the human body as a rigidly connected load [31], thereby neglecting the actual physical human–machine interactions arising from flexible contact, muscle compliance, and neural regulation [32]. Therefore, establishing an exoskeleton–human coupled dynamic model that accurately describes physical human–machine interactions is crucial for research on adaptive admittance controllers based on human–machine interaction forces [33]. In the coupled dynamics analysis of lower-limb exoskeletons, the exoskeleton is typically simplified to a two-bar linkage model, as shown in Figure 2. Therefore, based on Lagrange's method, a coupled dynamic model of the lower-limb exoskeleton-human–machine interaction system can be established, with its dynamic equations expressed as [34]:

$$M(\theta)\ddot{\theta} + C(\theta, \dot{\theta})\dot{\theta} + G(\theta) + f(\dot{\theta}) = \tau_h + \tau_{\text{int}} \tag{1}$$

Downloaded from https://www.cambridge.org/core. UNIVERSIDAD AUTONOMA METROPOLITANA, on 16 Nov 2026 at 03:23:03, subject to the Cambridge Core terms of use, available at https://www.cambridge.org/core/terms. https://doi.org/10.1017/S0263574726104056

In the equation, θ denotes the vector of joint angles for the lower limbs; $M(\theta) \in \mathbb{R}^{2\times2}$ is the positive-definite inertia matrix; $C(\theta) \in \mathbb{R}^{2\times2}$ represents the Coriolis and centrifugal force matrix; $G(\theta) \in \mathbb{R}^{2\times1}$ is the gravity vector; and $\tau_h = [\tau_{h_1}, \tau_{h_2}]^T$ represent the torques at the hip and knee joints of the exoskeleton, respectively, which can be measured via interaction force sensors. $\tau_{\text{int}} = [\tau_{\text{int}_1}, \tau_{\text{int}_2}]^T$ represent the elastic interaction torques at the thigh and shank cuffs, characterizing the human–robot interaction torque. The specific expression for the elastic interaction torque is $\tau_{\text{int}} = J^T F_{\text{int}}$, where F_{int} is the human–robot interaction force and $J^T \in \mathbb{R}^2$ is the Jacobian matrix; τ_h denotes the active torque exerted by the human subject.

Assuming the exoskeleton system parameters are unknown but bounded, the following properties hold:

Lemma 3.1. *The inertia matrix $M(\theta)$ is a symmetric, positive-definite, and bounded matrix.*

Lemma 3.2. *The matrix $\dot{M}(\theta) - 2C(\theta, \dot{\theta})$ is skew-symmetric, satisfying the following condition for any non-zero vector x*:

$$x^T[\dot{M}(\theta) - 2C(\theta, \dot{\theta})]x = 0 \tag{2}$$

Consequently, the resulting dynamic expression for the exoskeleton can be formulated as follows:

$$M = \begin{bmatrix} M_{11} & M_{12} \\ M_{21} & M_{22} \end{bmatrix}, C = \begin{bmatrix} C_{11} & C_{12} \\ C_{21} & C_{22} \end{bmatrix}, G = \begin{bmatrix} G_{11} \\ G_{21} \end{bmatrix} \tag{3}$$

where

$$\begin{cases} M_{11} = m_2 d_{sh}^2 + 2m_2 \cos(\theta_2) d_{sh} l_{th} + m_1 d_{th}^2 + m_2 l_{th}^2 + I_{sh} + I_{th} \\ M_{12} = m_2 d_{sh}^2 + l_{th} m_2 \cos(\theta_2) d_{sh} + I_{sh} \\ M_{21} = m_2 d_{sh}^2 + l_{th} m_2 \cos(\theta_2) d_{sh} + I_{sh} \\ M_{22} = m_2 d_{sh}^2 + I_{sh} \\ C_{11} = -d_{sh} l_{th} m_2 \dot{\theta}_2 \sin(\theta_2) \\ C_{12} = -d_{sh} l_{th} m_2 \sin(\theta_2)(\dot{\theta}_1 + \dot{\theta}_2) \\ C_{21} = d_{sh} l_{th} m_2 \dot{\theta}_1 \sin(\theta_2) \\ C_{22} = 0 \\ G_{11} = m_2 g[d_{sh} \sin(\theta_1 + \theta_2)] + l_{th} m_2 g \sin(\theta_1) + d_{th} m_1 g \sin(\theta_1) \\ G_{21} = d_{sh} m_2 g \sin(\theta_1 + \theta_2) \end{cases} \tag{4}$$

The aforementioned equations do not account for the influence of friction on the robot; however, in practical physical systems, friction is a critical variable. Therefore, we incorporate a well-established and universal friction model as follows:

$$f(\dot{\theta}) = \begin{bmatrix} f_{c1} \operatorname{sgn}(\dot{\theta}_1) + f_{v1} \dot{\theta}_1 \\ f_{c2} \operatorname{sgn}(\dot{\theta}_2) + f_{v2} \dot{\theta}_2 \end{bmatrix} \tag{5}$$

where $f_{c1} = 0.21$ and $f_{v1} = 0.36$ denote the Coulomb and viscous friction coefficients for the hip joint, respectively, and $f_{c2} = 0.06$ and $f_{v2} = 0.04$ represent the corresponding parameters for the knee joint.

4. Design of dual-layer adaptive admittance controller

4.1. Outer-loop admittance controller

In traditional admittance control methods, admittance parameters are typically treated as constants. However, in complex and time-varying dynamic environments, this approach imposes limitations on both control performance and adaptability. To better characterize human–robot interaction properties across different rehabilitation stages and to provide a foundation for subsequent adaptive adjustment of

Downloaded from https://www.cambridge.org/core. UNIVERSIDAD AUTONOMA METROPOLITANA, on 16 Nov 2026 at 03:23:03, subject to the Cambridge Core terms of use, available at https://www.cambridge.org/core/terms. https://doi.org/10.1017/S0263574726104056

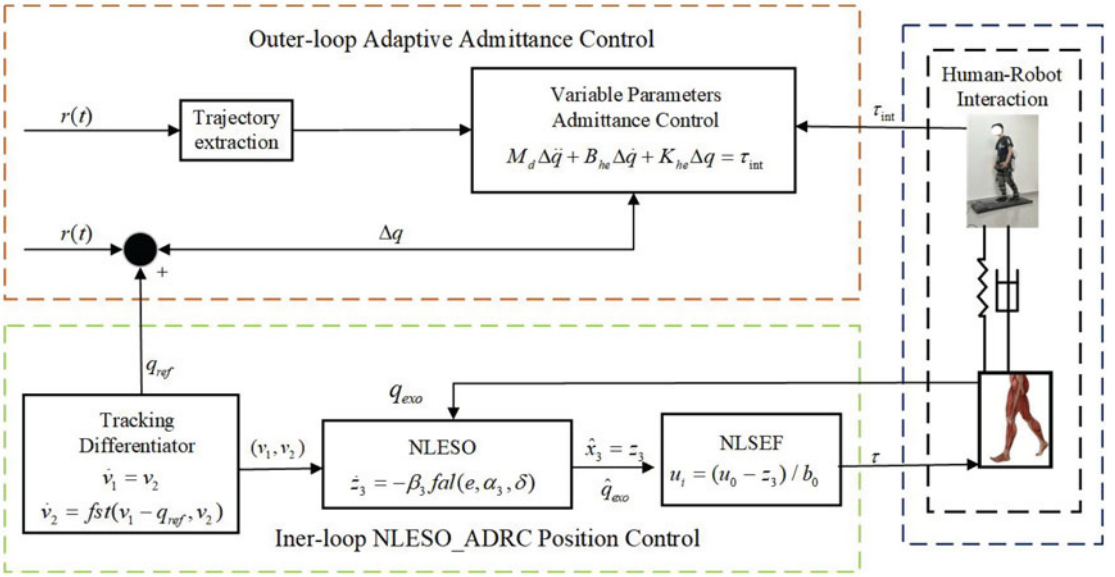


Figure 3. *Block diagram of two-layer adaptive admittance control.*

admittance parameters, this paper further designs a modified admittance model [35]:

$$M_d\Delta\ddot{q}(t) + B_d\Delta\dot{q}(t) + K_d\Delta q(t) = L(t)\tau_{\text{int}} \tag{6}$$

where $\Delta q(t) = q_r(t) - q_0(t)$. Here, q_0 is the desired trajectory of the exoskeleton, which also serves as the input to the inner-loop position control; q_r is the reference trajectory; and $L(t)$ is the modulation factor for tuning the admittance parameters, satisfying $L(t) \geq 0$.

To simplify the human-exoskeleton dynamics and simulate the interaction force, a spring-damper model is commonly adopted. Although this model serves as a fundamental approximation, it cannot fully capture pathological behaviors such as spasticity, fatigue, reflex reactions, or unpredictable autonomous movements. The mathematical model is expressed as [33]:

$$\tau_{\text{int}} = K_{he}(q_h - q_{exo}) + B_{he}(\dot{q}_h - \dot{q}_{exo}) \tag{7}$$

where $\tau_{\text{int}} = [\tau_{\text{hip}}, \tau_{\text{knee}}]^T$ is the interaction torque obtained in real-time via 1D force sensors, $q_h = [\theta_{h_1}, \theta_{h_2}]^T$ denotes the joint angles of the wearer, and $q_{exo} = [\theta_{exo_1}, \theta_{exo_2}]^T$ represents the joint angles of the exoskeleton robot. The parameter matrices $K_{he} = \text{diag}(K_{he_1}, K_{he_2})$ and $B_{he} = \text{diag}(B_{he_1}, B_{he_2})$ represent the stiffness and damping coefficient matrices, respectively, where subscripts 1 and 2 denote the hip and knee joints. The overall system control architecture is illustrated in Figure 3.

4.2. Dual-layer adaptive regulation mechanism

Traditional admittance control methods rely heavily on empirical settings for admittance parameters. Once these parameters are determined, it is difficult for the system to dynamically adjust them during the training process in response to changes in gait rhythm and human–robot interaction states. Therefore, to ensure that the exoskeleton control system provides appropriate assistance and compliant adjustment effects under varying walking speeds, this paper proposes a Dual-layer Adaptive Admittance Control (DAAC) strategy. The outer layer of this strategy sets baseline admittance parameters according to different walking speed gears to accommodate the variations in movement characteristics under low, medium, and high-speed walking conditions. Meanwhile, the inner layer continuously performs adaptive adjustments to the damping and stiffness parameters based on real-time interaction torques and admittance correction terms, thereby enhancing the system's compliance and stability across different gait rhythms.

Downloaded from https://www.cambridge.org/core. UNIVERSIDAD AUTONOMA METROPOLITANA, on 16 Nov 2026 at 03:23:03, subject to the Cambridge Core terms of use, available at https://www.cambridge.org/core/terms. https://doi.org/10.1017/S0263574724104056

In this paper, three display speed gears for the treadmill are established, denoted as $v_{\text{disp}} \in \{2, 4, 6\}$. Considering the mapping relationship between the treadmill's displayed speed and the actual walking speed, the actual walking speed can be expressed as:

$$v_{\text{act}}^{(s)} = k\, v_{\text{disp}}^{(s)} \tag{8}$$

where $v_{\text{disp}}^{(s)}$ represents the displayed speed at the s-th speed gear, $v_{\text{act}}^{(s)}$ is the corresponding actual walking speed, and $k = 0.6$ is the speed conversion factor. Based on these three speed gears, the walking condition index w is defined as:

$$w = \begin{cases} 1, & v_{\text{disp}} = 2\ \text{km/h} \\ 2, & v_{\text{disp}} = 4\ \text{km/h} \\ 3, & v_{\text{disp}} = 6\ \text{km/h} \end{cases} \tag{9}$$

Here, $w = 1$ corresponds to the low-speed walking condition, primarily representing slow-speed rehabilitation gait; $w = 2$ denotes the medium-speed walking condition, reflecting a normal walking rhythm; and $w = 3$ represents the higher-speed walking condition, used to characterize gait variations during high-speed brisk walking. These three speed gears cover the walking range from slow rehabilitation to high-speed brisk walking, which allows for the analysis of the adaptability and stability of the proposed control method under different exercise intensities.

The aforementioned speed gear regulation provides appropriate baseline admittance parameters for different walking rhythms; however, actual human–robot interaction is determined by more than just walking speed. Under the same speed condition, the subject's active participation, gait fluctuations, interaction torques, and trajectory-tracking errors still vary in real time. Therefore, relying solely on fixed speed-based parameters is insufficient to meet the dynamic requirements for system compliance and stability.

To this end, building upon the baseline parameters derived from the outer-layer gait speed gears, this paper further designs an inner-layer adaptive admittance parameter update law. To characterize the interaction state of the current control system, the following interaction state indices are introduced. For the i-th joint of the lower-limb exoskeleton, the interaction state variables are defined as:

$$\begin{cases} \tau_i = |\tau_{\text{int}_i}| \\ e_i = |\Delta q_i| \end{cases} \tag{10}$$

Based on the variables defined above, the interaction excitation function is constructed as follows:

$$\Phi_i(\tau_i, e_i) = \max\left(0, \frac{\tau_i - \tau_{\text{th}_i}}{\tau_{\text{th}_i}}\right) + \max\left(0, \frac{e_i - e_{\text{th}_i}}{e_{\text{th}_i}}\right) \tag{11}$$

The τ_{th_i} denotes the interaction torque threshold for the i-th joint, and e_{th_i} represents the threshold for the admittance correction term.

The adaptive learning rate vectors for damping and stiffness are defined as φ_{B_i} and φ_{K_i}, respectively. Their continuous-time adaptive laws are designed as follows:

$$\begin{cases} \dot{\varphi}_{B_i} = \alpha_{B_i}\Phi_i(\tau_i, e_i) - \beta_{B_i}\varphi_{B_i} \\ \dot{\varphi}_{K_i} = \alpha_{K_i}\Phi_i(\tau_i, e_i) - \beta_{K_i}\varphi_{K_i} \end{cases} \tag{12}$$

And $\alpha_{(\cdot)} > 0$ represents the learning rate growth coefficient, which regulates the response speed of the admittance parameters to changes in the interaction state. This parameter should not be excessively large to avoid rapid fluctuations in admittance parameters. Meanwhile, $\beta_{(\cdot)} > 0$ denotes the learning rate decay coefficient, which ensures that the learning variables gradually attenuate once the interaction excitation weakens. These coefficients must be selected in conjunction with the permissible range of the admittance parameters.

To ensure that the learning rates remain bounded, the following constraint (12) is satisfied:

$$\varphi_{\min} \leq \varphi_{B_i}, \varphi_{K_i} \leq \varphi_{\max} \tag{13}$$

Downloaded from https://www.cambridge.org/core. UNIVERSIDAD AUTONOMA METROPOLITANA, on 16 Nov 2026 at 03:23:03, subject to the Cambridge Core terms of use, available at https://www.cambridge.org/core/terms. https://doi.org/10.1017/S0263574726104056

Accordingly, the dynamic adjustment of admittance parameters based on the learning rates is formulated as follows:

$$\begin{cases} B_{d_i}(k) = \mathrm{sat}_{[B_{\min_i}, B_{\max_i}]}[B_{0_i}^{(s)} + \Gamma_{B_i}\varphi_{B_i}(k)|\Delta\dot{\theta}|] \\ K_{d_i}(k) = \mathrm{sat}_{[K_{\min_i}, K_{\max_i}]}[K_{0_i}^{(s)} + \Gamma_{K_i}\varphi_{K_i}(k)|\Delta\dot{\theta}|] \end{cases} \tag{14}$$

where $B_{0_i}^{(s)}$ and $K_{0_i}^{(s)}$ represent the baseline damping and stiffness of the i-th joint under the s-th walking speed condition, respectively; $\Gamma_{B_i} > 0$ and $\Gamma_{K_i} > 0$ are the admittance parameter adjustment gains; and $\mathrm{sat}_{[\cdot]}$ denotes the saturation function.

Furthermore, to ensure system stability and compliance, the admittance parameters must satisfy the following constraints:

$$B_{\min_i} \le B_{d_i} \le B_{\max_i}, \quad K_{\min_i} \le K_{d_i} \le K_{\max_i} \tag{15}$$

where $B_{\min_i}, K_{\min_i} > 0$. These constraints ensure the positive definiteness of the virtual damping and stiffness matrices:

$$B_d = B_d^T(t) > 0, \quad K_d = K_d^T(t) > 0 \tag{16}$$

This design ensures the stability and smoothness of the outer-loop admittance correction process, while providing continuous and reasonable references for the inner-loop trajectory-tracking control. The stability of the outer-loop adaptive admittance control is proved using Lyapunov's stability theorem as follows. In addition to the requirement that the virtual damping matrix and virtual stiffness matrix remain positive definite, the mass matrix is also assumed to satisfy the following condition:

$$M_d = M_d^T > 0 \tag{17}$$

First, assuming that τ_{int} is bounded and slowly varying, the stability of the adaptive admittance control system is primarily determined by B_d and K_d. Next, choose the Lyapunov function V_1 as follows:

$$V_1 = \frac{1}{2}\Delta\dot{q}^T M_d \Delta\dot{q} + \frac{1}{2}\Delta q^T K_d \Delta q \tag{18}$$

Taking the time derivative, we have:

$$\dot{V}_1 = \Delta\dot{q}^T M_d \Delta\ddot{q} + \frac{1}{2}\Delta q^T \dot{K}_d \Delta q + \Delta\dot{q}^T K_d \Delta q \tag{19}$$

Substituting the above equation, we obtain:

$$\dot{V}_1 = \Delta\dot{q}^T B_d \Delta\dot{q} + \Delta\dot{q}^T L(t)\tau_{\mathrm{int}} + \frac{1}{2}\Delta q^T \dot{K}_d \Delta q \tag{20}$$

If there exists a constant $k_c > 0$ such that:

$$\|\dot{K}_d\| \le k_c \tag{21}$$

Then, we have:

$$\dot{V}_1 \le -\lambda_{\min}(B_d)\|\Delta\dot{q}\|^2 + \|\Delta\dot{q}\|\|L(t)\tau_{\mathrm{int}}\| + \frac{1}{2}k_c\|\Delta q\|^2 \tag{22}$$

When τ_{int}, $K_d(t)$, $B_d(t)$, and $\dot{K}_d(t)$ are all bounded, the admittance correction terms Δq and $\Delta\dot{q}$ are ultimately uniformly bounded.

5. Inner-loop robust control based on NLESO-ADRC

However, the outer loop only facilitates the online adjustment of the reference trajectory and cannot guarantee that the exoskeleton joints accurately execute this trajectory. Due to factors such as nonlinear coupling, parameter uncertainties, friction disturbances, and human–robot interaction disturbances within the lower-limb exoskeleton system, the actual joint angles may still exhibit tracking errors and response delays if the inner-loop controller lacks sufficient robustness.

Downloaded from https://www.cambridge.org/core. UNIVERSIDAD AUTONOMA METROPOLITANA, on 16 Nov 2026 at 03:23:03, subject to the Cambridge Core terms of use, available at https://www.cambridge.org/core/terms. https://doi.org/10.1017/S0263574726104056

Therefore, to improve the tracking accuracy and disturbance rejection capability of the exoskeleton joints regarding the corrected reference trajectory, this paper further designs an inner-loop ADRC based on an NLESO [19].

The outer-loop adaptive admittance controller generates the corrected reference trajectory $q_r(t)$, with its first and second derivatives denoted as $\dot{q}_r(t)$ and $\ddot{q}_r(t)$, respectively. The objective of the inner-loop controller is to enable the actual joint angles $q(t)$ of the exoskeleton to accurately track this reference trajectory.

For the i-th joint (where $i = 1$ denotes the hip joint and $i = 2$ denotes the knee joint), the state variables are defined as:

$$\begin{cases} x_{1_i} = q_i \\ x_{2_i} = \dot{q}_i \end{cases} \tag{23}$$

The dynamics of the i-th joint can be equivalently represented as the following second-order system:

$$\begin{cases} \dot{x}_{1_i} = x_{2_i} \\ \dot{x}_{2_i} = F_i(x,t) + b_i u_i \end{cases} \tag{24}$$

Here, u_i is the control input for the i-th joint, b_i represents the actual control gain, and $F_i(x,t)$ denotes the nonlinear dynamics and uncertainty terms of the system. Because the actual control gain b_i is difficult to obtain precisely in practical systems, a nominal control gain $b_{0_i} > 0$ is introduced. By incorporating the control gain deviation into the total disturbance term, the aforementioned equation can be rewritten as:

$$\dot{x}_{2_i} = d_i(x,t) + b_{0_i} u_i \tag{25}$$

where:

$$d_i(x,t) = F_i(x,t) + (b_i - b_{0_i}) u_i \tag{26}$$

where $d_i(x,t)$ represents the total disturbance of the i-th joint, encompassing unmodeled dynamics, parameter uncertainties, joint coupling terms, friction errors, human–robot interaction disturbances, and control gain deviations. We define the extended state as:

$$x_{3_i} = d_i(x,t) \tag{27}$$

Consequently, the extended state model is formulated as:

$$\begin{cases} \dot{x}_{1_i} = x_{2_i} \\ \dot{x}_{2_i} = x_{3_i} + b_{0_i} u_i \\ \dot{x}_{3_i} = \dot{d}_i(x,t) \end{cases} \tag{28}$$

Define the observation error as:

$$e_{0_i} = z_{1_i} - y_i \tag{29}$$

To improve the convergence speed of the observer during the large-error phase and suppress chattering during the small-error phase, a nonlinear function is introduced:

$$fal(e,\alpha,\delta) = \begin{cases} |e|^{\alpha} \operatorname{sgn}(e), & |e| > \delta \\ \dfrac{e}{\delta^{1-\alpha}}, & |e| \le \delta \end{cases} \tag{30}$$

where $0 < \alpha < 1$ and $\delta > 0$. Furthermore, for the i-th joint, let the reference trajectory generated by the outer-loop admittance controller be q_{r_i}, with its first and second derivatives denoted as $\dot{q}_{r_i}$ and $\ddot{q}_{r_i}$, respectively. Define the tracking error as:

$$\begin{cases} e_{1_i} = z_{1_i} - q_{r_i} \\ e_{2_i} = z_{2_i} - \dot{q}_{r_i} \end{cases} \tag{31}$$

Based on the tracking errors defined earlier, the intermediate control law is designed as:

$$u_{0_i} = \ddot{q}_{r_i} - k_{1_i} e_{1_i} - k_{2_i} e_{2_i}. \tag{32}$$

Downloaded from https://www.cambridge.org/core. UNIVERSIDAD AUTONOMA METROPOLITANA, on 16 Nov 2026 at 03:23:03, subject to the Cambridge Core terms of use, available at https://www.cambridge.org/core/terms. https://doi.org/10.1017/S0263574726104056

where ($k_{1_i} > 0$) and ($k_{2_i} > 0$) are the inner-loop feedback control gains. The gain (k_{1_i}) mainly affects the convergence speed of the position tracking error, although (k_{2_i}) mainly affects the damping characteristic of the velocity tracking error. In the parameter selection process, a trade-off should be made among tracking accuracy, control torque amplitude, and response smoothness, so as to avoid excessive feedback gains causing drastic variations in the control input.

To compensate for the lumped disturbance of the system, the disturbance estimate z_{3_i} obtained by the NLESO is introduced into the control law. The final control input is given by

$$u_i = \frac{\ddot{q}_{r_i} - k_{1_i}e_{1_i} - k_{2_i}e_{2_i} - z_{3_i}}{b_{0_i}}, \tag{33}$$

where $b_{0_i} > 0$ is the nominal control gain of the i-th joint. Through the compensation term z_{3_i}, the effects of unmodeled dynamics, parameter uncertainties, friction errors, interaction disturbances, and control gain deviations can be actively estimated and compensated for, thereby improving the trajectory-tracking accuracy and disturbance rejection capability of the inner-loop controller.

In matrix form:

$$\dot{e}_i = A_i e_i + B_i \tilde{x}_{3_i} \tag{34}$$

When $k_{1,i} > 0$ and $k_{2,i} > 0$, the matrix A_i is a Hurwitz matrix. For any positive definite matrix $Q_i = Q_i^T > 0$, there exists a unique positive definite matrix $P_i = P_i^T > 0$ satisfying

$$A_i^T P_i + P_i A_i = -Q_i. \tag{35}$$

Then, the Lyapunov function is selected as

$$V_i = e_i^T P_i e_i. \tag{36}$$

Taking the derivative of V_i yields

$$\dot{V}_i = -e_i^T Q_i e_i + 2e_i^T P_i B_i \tilde{x}_{3_i}. \tag{37}$$

If the NLESO can guarantee that the disturbance estimation error is bounded, there exists a positive constant $\delta_i > 0$ such that

$$|\tilde{x}_{3_i}| \le \delta_i. \tag{38}$$

Then, the derivative of the Lyapunov function satisfies

$$\dot{V}_i \le -\lambda_{\min}(Q_i) \|e_i\|^2 + 2 \|P_i B_i\| \delta_i \|e_i\|. \tag{39}$$

Therefore, when

$$\|e_i\| > \frac{2 \|P_i B_i\| \delta_i}{\lambda_{\min}(Q_i)}, \tag{40}$$

we have

$$\dot{V}_i < 0. \tag{41}$$

Thus, the closed-loop tracking errors $e_{1,i}$ and $e_{2,i}$ are uniformly ultimately bounded.

6. Experimental validation and discussion

6.1. Experimental method

To verify the effectiveness of the proposed method, experiments were conducted using the lower-limb exoskeleton experimental platform described in the previous sections. Six healthy subjects were recruited for the experiment. This study was approved by the Ethics Committee of the Institute of Biomedical Research, Anhui University of Science and Technology (Approval No. 2023-5). Figure 4 shows the experimental process of Subject 3, and the basic information of all recruited subjects is presented in Table I.

Downloaded from https://www.cambridge.org/core. UNIVERSIDAD AUTONOMA METROPOLITANA, on 16 Nov 2026 at 03:23:03, subject to the Cambridge Core terms of use, available at https://www.cambridge.org/core/terms. https://doi.org/10.1017/S0263574726104056

Table I. *Basic information of the subjects.*

Subject	Gender	Height/cm	Weight/kg
1	Female	175	58
2	Male	185	80
3	Male	183	70
4	Male	180	70
5	Male	181	68
6	Male	178	66



Figure 4. *Experimental procedure for subject 3.*

To evaluate the performance of the proposed control model under different walking rhythms, three treadmill speed levels were used in the experiment, namely 1.2, 2.4, and 3.6 km/h. Considering the relationship between the displayed treadmill speed and the corresponding converted actual walking speed, both the treadmill display values and their corresponding actual speeds were used to describe the experimental conditions in this study.

The three speed levels cover a walking range from low-speed rehabilitation gait to moderate- and relatively high-speed walking and can reflect the gait variation characteristics of the human body under different movement intensities. Therefore, they are suitable for analyzing the adaptability and stability of the proposed model under different walking-speed conditions.

To ensure the consistency and reliability of data acquisition under different speed conditions, a unified experimental procedure was adopted. With the assistance of the operator, each subject first wore the lower-limb exoskeleton and stood still on the treadmill before the experiment started. At each speed level, the subject first walked on the treadmill at the current preset speed for 2–3 min to adapt to the corresponding walking rhythm. After the gait became relatively stable, 30–60 s of continuous walking data were collected. To reduce the influence of unstable gait during the start and stop stages on data quality, the data corresponding to the initial start-up and final stopping stages were removed during formal modeling and analysis. However, the intermediate transition stage from slow movement to static standing was retained, together with the stable walking interval, to form a complete experimental process. For each speed level, data acquisition was repeated two to three times, with an interval of approximately 1 min between repeated trials. Before switching to the next speed level, the subject rested for 1–2 min to reduce the influence of fatigue on subsequent experimental data. Figure 5 shows three groups of right-leg experimental data from Subject 3.

6.2. Simulation experiment

The simulation was conducted in MATLAB/Simulink. Since the experimental process lasted for a relatively long period, a unified preset switching time was adopted to ensure that different controllers were compared under identical walking-speed conditions. Specifically, 10 s of experimental data were selected from each walking-speed stage, and a complete input trajectory was reconstructed according to

Downloaded from https://www.cambridge.org/core. UNIVERSIDAD AUTONOMA METROPOLITANA, on 16 Nov 2026 at 03:23:03, subject to the Cambridge Core terms of use, available at https://www.cambridge.org/core/terms. https://doi.org/10.1017/S0263574726104056

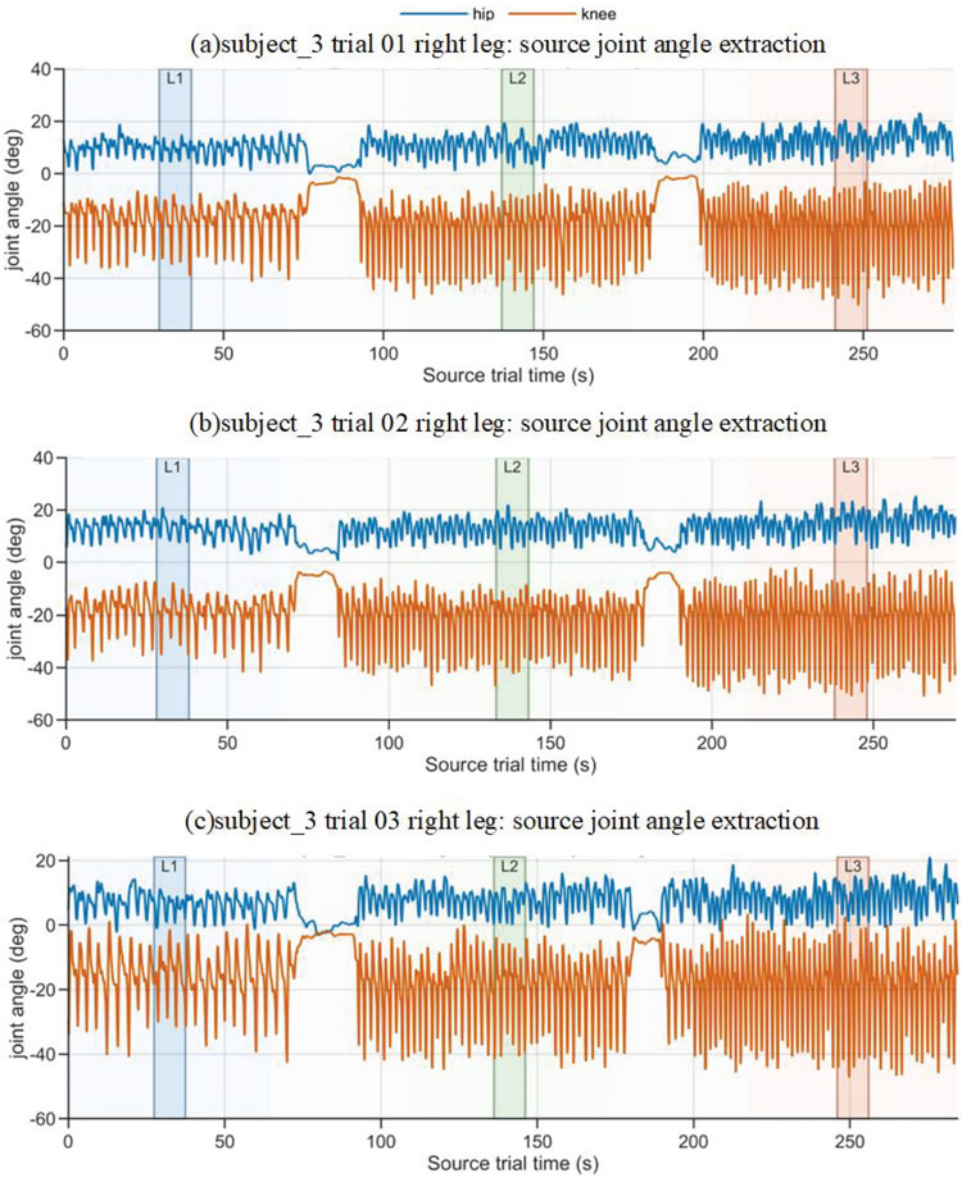


Figure 5. *Experimental data of subject 3.*

the experimental procedure described earlier. The reconstructed trajectory was then used as the simulation input. In this study, one dataset was selected from the collected subject data for simulation validation. As shown in Figure 6, the second trial of Subject 3 was used for the simulation analysis.

The simulation parameters were designed based on the body size parameters of the exoskeleton wearer and the actual structural parameters of the lower-limb exoskeleton, as shown in Table II.

6.3. Performance comparison

To verify the effectiveness of the proposed control method, a hierarchical comparison strategy is adopted in this section to analyze the performance of the control system.

Downloaded from https://www.cambridge.org/core. UNIVERSIDAD AUTONOMA METROPOLITANA, on 16 Nov 2026 at 03:23:03, subject to the Cambridge Core terms of use, available at https://www.cambridge.org/core/terms. https://doi.org/10.1017/S0263574726104056

Table II. *Simulation parameters of the exoskeleton system.*

Parameters (unit)	value
m_1/kg	3.2835
m_2 /kg	3.2835
l_{th}/m	0.420
l_{sh}/m	0.375
d_{th}/m	0.193
d_{sh}/m	0.143
I_{th}/kg·m^2	0.059
I_{sh}/kg·m^2	0.046

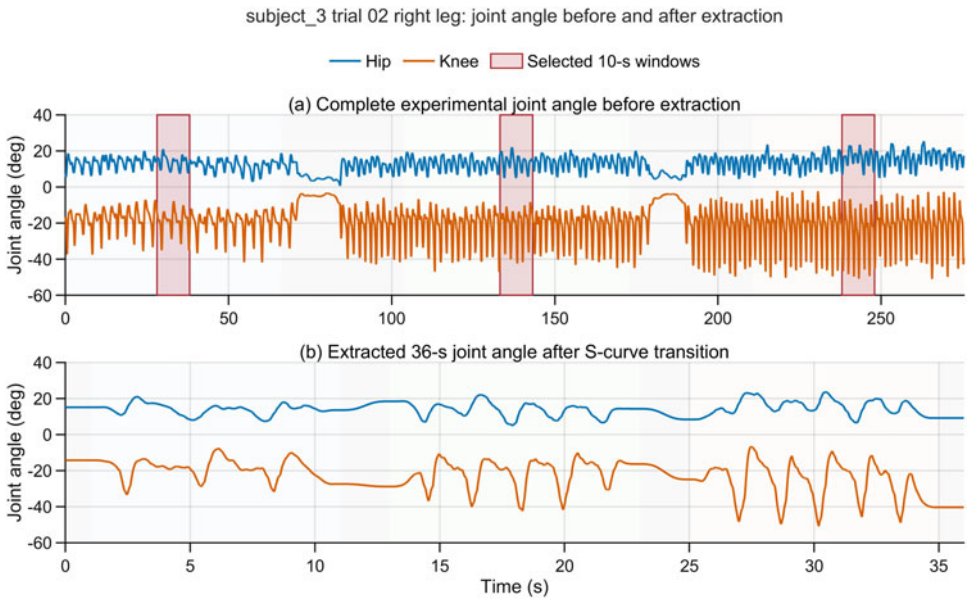


Figure 6. *Experimental input reference trajectory.*

6.3.1. Inner-loop performance comparison

To verify the effectiveness of the NLESO-ADRC inner-loop controller adopted in this paper, the inner-loop performance is compared under the condition that the outer-loop admittance parameters remain the same. Specifically, the fixed admittance control method is uniformly used in the outer loop, whereas three inner-loop control methods, namely PID, LESO-ADRC, and NLESO-ADRC, are selected for simulation comparison. These three controller combinations are denoted as F-PID, F-LESO, and F-NLESO, respectively.

To ensure the fairness of the comparison across different subjects and controllers, a unified set of controller parameters was employed for all experimental groups. Parameter tuning was performed using an offline step-by-step heuristic approach, adhering to consistent tuning principles. The parameters remained unchanged for all six subjects, with no individual tuning performed to account for inter-subject differences. For the baseline methods, the LESO-ADRC and NLESO-ADRC shared identical feedback gains and observer bandwidths, with only the error feedback form of the extended state observer being modified. Similarly, the PID controller and the ADRC controller utilized consistent proportional and derivative gains. The detailed control parameters are summarized in Table III.

Downloaded from https://www.cambridge.org/core. UNIVERSIDAD AUTONOMA METROPOLITANA, on 16 Nov 2026 at 03:23:03, subject to the Cambridge Core terms of use, available at https://www.cambridge.org/core/terms. https://doi.org/10.1017/S0263574726104056

Table III. *Inner-loop different control parameters.*

Parameters	Hip joint	Knee joint	Unit
K_p	46.9594	37.8654	s^{-2}
K_d	19.1751	30.3696	s^{-1}
ω_o	9.3714	10.4551	rad/s
γ_d	0.6890	0.5796	–
α_1	1.0000	1.0000	–
α_2	0.8200	0.8200	–
α_3	0.6200	0.6200	–
δ	0.1000	0.1000	–
D	0.0854	0.0854	s

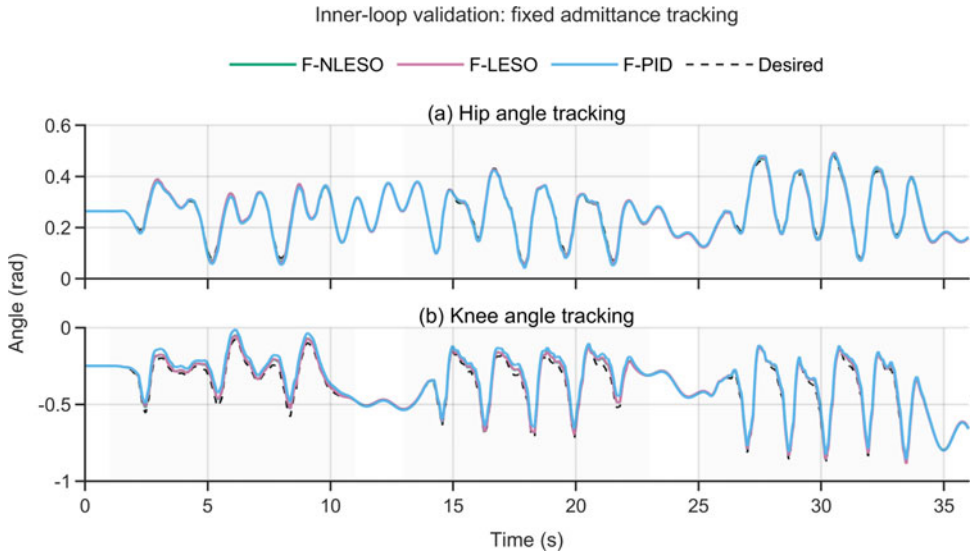


Figure 7. *Trajectory-tracking results of the inner-loop under fixed admittance conditions.*

As can be seen from Figure 7(a) and (b), all three control methods can achieve basic tracking of the desired trajectories during the hip and knee joint angle-tracking processes; however, significant differences appear during the rapid variation phases of the trajectories. During the intervals of 3–10, 15–22, and 28–34 s, the F-PID controller exhibits noticeable tracking lag and deviation in both the hip and knee joints, indicating that the system's adaptability to dynamic trajectory changes and disturbances is relatively limited when utilizing only a PID inner loop. In contrast, both F-LESO and F-NLESO remain closer to the desired trajectories, suggesting that the introduction of an ESO has effectively enhanced the system's dynamic compensation capability. Furthermore, F-NLESO performs slightly better than F-LESO at certain peaks and transition positions, demonstrating that the NLESO-ADRC inner loop possesses superior dynamic response and tracking accuracy when handling complex motion trajectories.

To further evaluate the tracking performance of different inner-loop controllers, Figure 8 presents a comparison of the tracking errors for both the hip and knee joints. It can be observed that the magnitude of the hip joint tracking error for F-PID is generally greater than that of F-LESO and F-NLESO, whereas the error curves of the latter two remain significantly closer to the zero axis. The differences between the controllers are even more pronounced in the knee joint error plots. The F-PID error reaches approximately 0.08–0.10 rad at several stages, indicating that the PID inner loop lacks sufficient adaptability to the knee joint trajectory, which is characterized by larger variation amplitudes and stronger dynamic features. In contrast, the knee joint errors for F-LESO and F-NLESO are markedly reduced and maintained

Downloaded from https://www.cambridge.org/core. UNIVERSIDAD AUTONOMA METROPOLITANA, on 16 Nov 2026 at 03:23:03, subject to the Cambridge Core terms of use, available at https://www.cambridge.org/core/terms. https://doi.org/10.1017/S0263574726104056

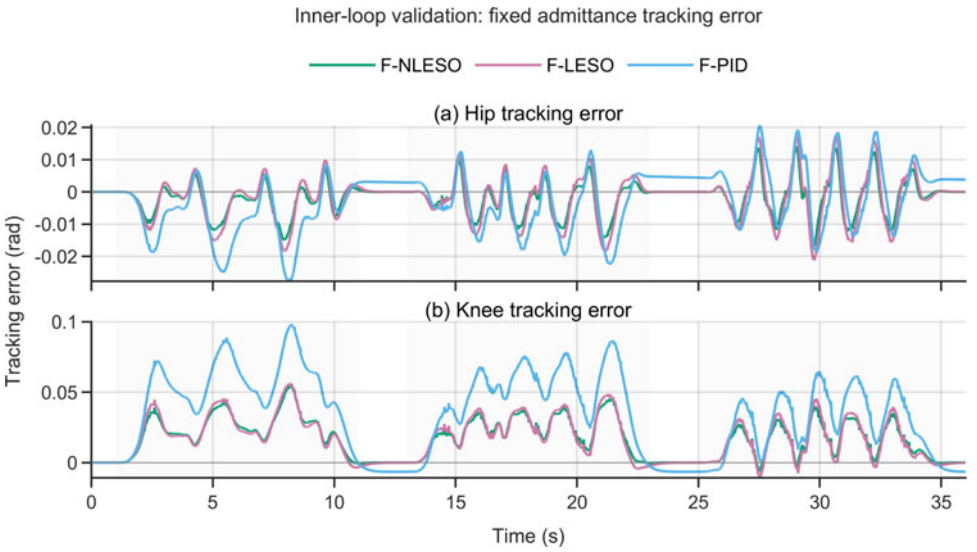


Figure 8. *Trajectory-tracking errors of the inner-loop under fixed admittance conditions.*

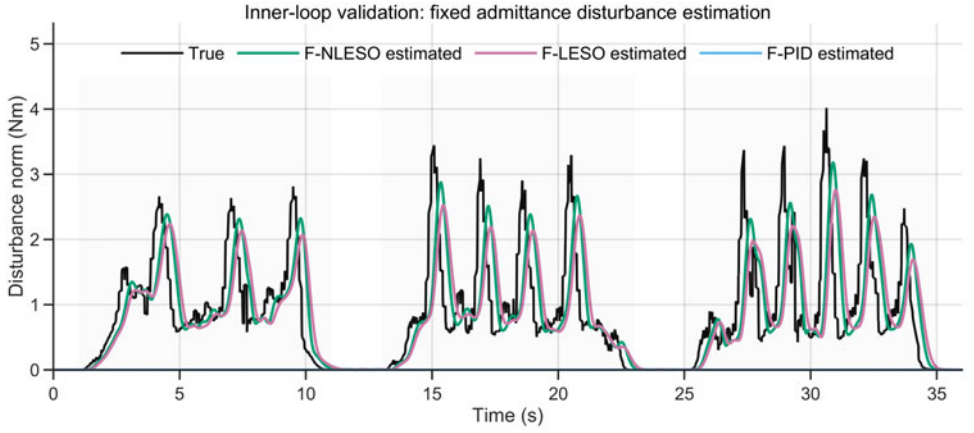


Figure 9. *Disturbance norm estimation under fixed admittance conditions.*

within a much smaller range. Furthermore, the F-NLESO error curve is consistently lower than that of the F-LESO, with smaller fluctuations during peak stages. This confirms that the NLESO-ADRC inner loop further improves the trajectory-tracking accuracy and dynamic response stability of the system.

Figures 9 and 10 show the disturbance estimation results and estimation errors for the different inner-loop controllers under fixed admittance conditions, respectively. As shown in Figure 9, the actual disturbance exhibits significant peaks during multiple motion phases. Because the F-PID controller lacks a disturbance observation mechanism, its estimated disturbance remains close to zero and fails to capture the variations in the actual disturbance. In contrast, both F-LESO and F-NLESO effectively track the trend of the actual disturbance and generate corresponding responses during peak phases, demonstrating that the ESO can achieve online estimation of the system's total disturbance.

Further analysis of Figure 10 reveals that the F-PID controller exhibits large estimation errors during the disturbance variation phases for both the hip and knee joints, with a particularly significant negative bias in the knee joint, indicating limited compensation capability under external disturbances and model uncertainties. The estimation error magnitudes for both F-LESO and F-NLESO are significantly reduced and confined to a smaller range, confirming their superior disturbance estimation capabilities. Notably, the F-NLESO exhibits smaller error fluctuations during phases of abrupt disturbance changes, indicating

Downloaded from https://www.cambridge.org/core. UNIVERSIDAD AUTONOMA METROPOLITANA, on 16 Nov 2026 at 03:23:03, subject to the Cambridge Core terms of use, available at https://www.cambridge.org/core/terms. https://doi.org/10.1017/S0263574726104056

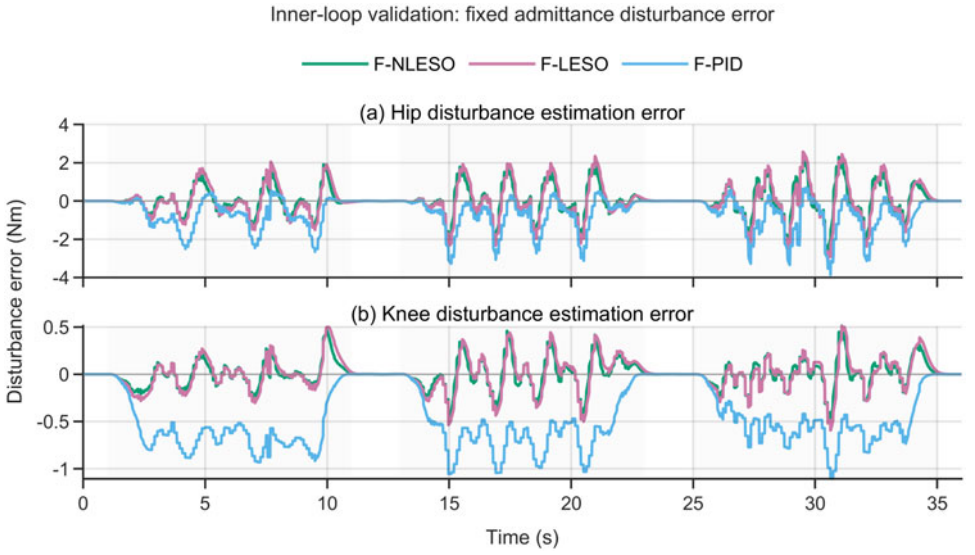


Figure 10. *Disturbance estimation error under fixed admittance conditions.*

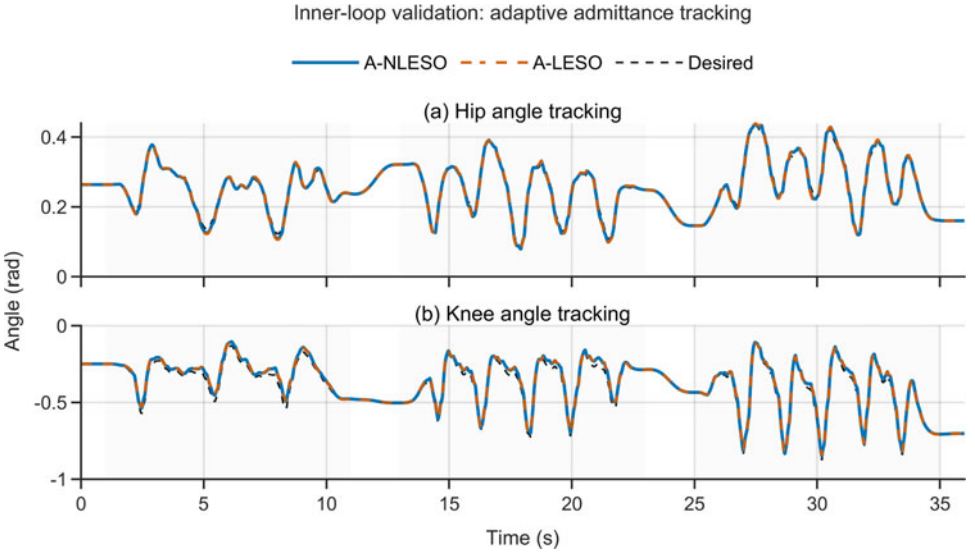


Figure 11. *Inner-loop trajectory-tracking results under adaptive admittance conditions.*

that the NLESO offers higher estimation accuracy and robustness against time-varying disturbances and nonlinear dynamic variations.

The aforementioned comparative results under fixed admittance conditions demonstrate that, with the outer-loop parameters held constant, the NLESO-ADRC controller achieves superior trajectory-tracking precision and disturbance estimation capability compared with both PID and LESO controllers. Given that the LESO outperforms the PID controller across all performance metrics, and considering that the proposed control framework ultimately incorporates an adaptive admittance outer loop, this study further evaluates the applicability of the NLESO-ADRC under the final outer-loop strategy. Consequently, we proceed to compare the LESO and NLESO-ADRC inner-loop control methods – denoted as A-LESO and A-NLESO, respectively – within the context of the adaptive admittance outer loop.

Figures 11 and 12 present the joint angle-tracking results and tracking errors of the different inner-loop controllers under adaptive admittance conditions, respectively. As shown in Figure 11,

Downloaded from https://www.cambridge.org/core. UNIVERSIDAD AUTONOMA METROPOLITANA, on 16 Nov 2026 at 03:23:03, subject to the Cambridge Core terms of use, available at https://www.cambridge.org/core/terms. https://doi.org/10.1017/S0263574726104056

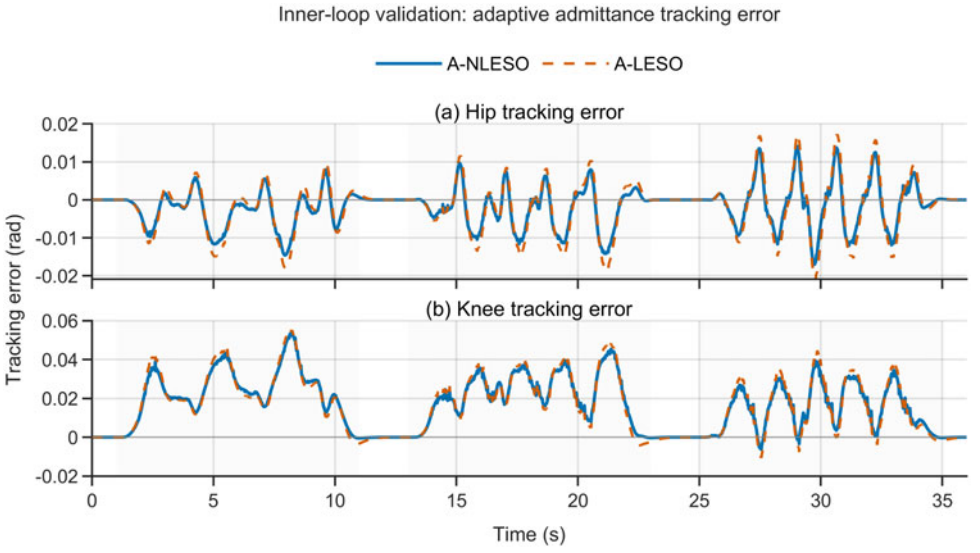


Figure 12. *Inner-loop trajectory-tracking errors under adaptive admittance conditions.*

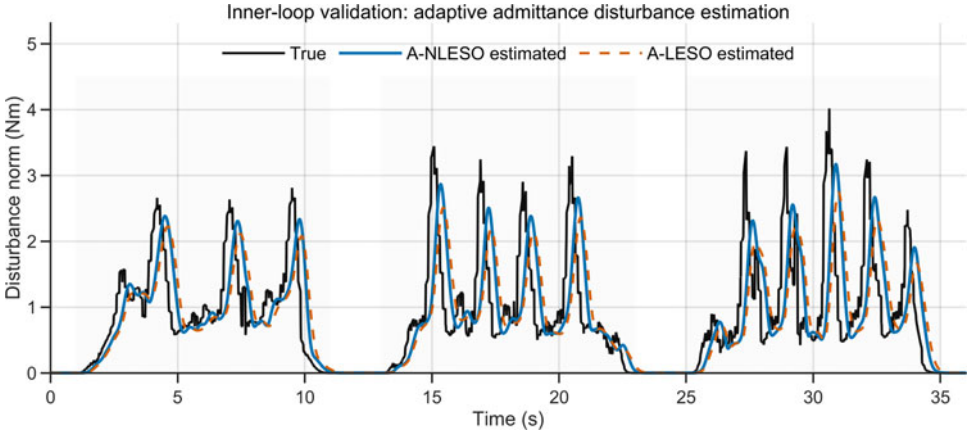


Figure 13. *Disturbance norm estimation under adaptive admittance conditions.*

both A-LESO and A-NLESO effectively follow the desired hip and knee joint trajectories, with the actual curves remaining largely consistent with the desired ones, indicating that the integration of the adaptive admittance outer loop with observer-based inner-loop controllers ensures stable system operation. Notably, the A-NLESO demonstrates a tracking performance closer to the desired trajectory, particularly at the peak and valley positions of the knee joint.

Further analysis of Figure 12 reveals that the hip joint-tracking errors for both methods are generally maintained within the range of ± 0.02 rad, and the knee joint errors are primarily concentrated within ± 0.05 rad, confirming that both methods achieve high trajectory-tracking precision. Compared with the A-LESO, the A-NLESO exhibits smaller error fluctuations during phases of rapid trajectory variation and peak transitions, demonstrating that the NLESO-ADRC inner loop possesses superior dynamic tracking performance under adaptive admittance conditions.

The improvement in trajectory-tracking error is closely related to the disturbance estimation and compensation capabilities of the inner-loop controllers. Figure 13 illustrates the disturbance estimation results for the two inner-loop controllers under adaptive admittance conditions. It can be observed that both A-LESO and A-NLESO effectively follow the trends of the actual disturbances and generate corresponding responses during peak phases, indicating that both observers possess online disturbance

Downloaded from https://www.cambridge.org/core. UNIVERSIDAD AUTONOMA METROPOLITANA, on 16 Nov 2026 at 03:23:03, subject to the Cambridge Core terms of use, available at https://www.cambridge.org/core/terms. https://doi.org/10.1017/S0263574726104056

Table IV. *Quantitative comparison of tracking, estimation, and admittance correction indices.*

Control method	Hip RMS (rad)	Knee RMS (rad)	Avg. RMS (rad)	Hip RMSE (Nm)	Knee RMSE (Nm)	Avg. RMSE (Nm).
F-PID	0.009536	0.044259	0.032014	1.055603	0.551848	0.842269
F-LESO	0.007079	0.022690	0.016807	0.889102	0.173443	0.640541
F-NLESO	0.005602	0.021776	0.015899	0.767788	0.147615	0.552851
A-LESO	0.007031	0.022547	0.016700	0.886467	0.173079	0.638663
A-NLESO	0.005563	0.021641	0.015800	0.765757	0.147419	0.551414

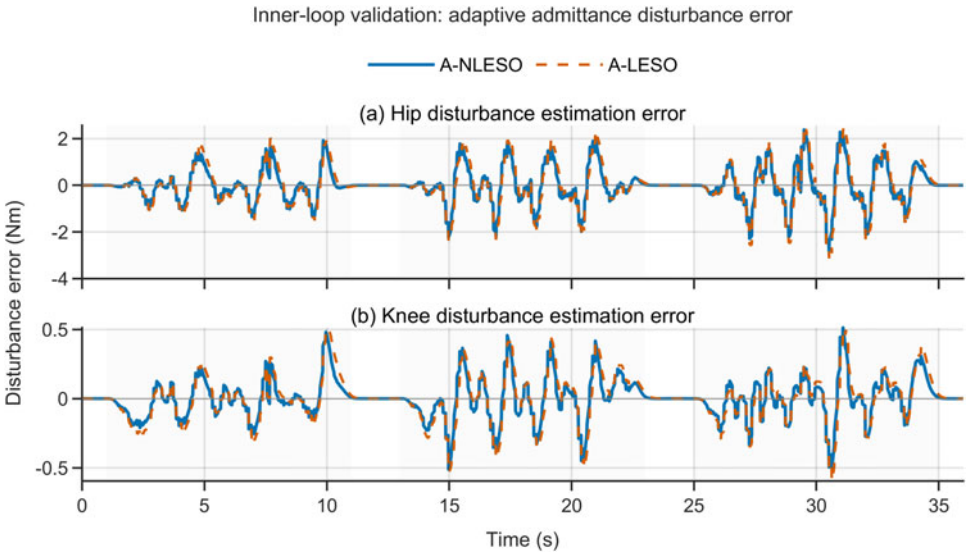


Figure 14. *Disturbance estimation error under adaptive admittance conditions.*

estimation capabilities. In comparison, the A-NLESO yields estimates closer to the actual disturbances at several peak locations, such as 15 s, 20 s, and the 30–33 s interval, whereas the A-LESO exhibits a certain degree of amplitude attenuation and response lag.

Further analysis of Figure 14 shows that the hip joint disturbance estimation errors for both methods are generally maintained within the range of ± 2 Nm, although the knee joint errors are primarily concentrated within ± 0.5 Nm, confirming that both controllers achieve high estimation precision. However, during phases of disturbance peaks and rapid transitions, the A-LESO exhibits more pronounced error fluctuations and lag phenomena. In contrast, the A-NLESO maintains relatively smaller errors, demonstrating its more timely response to time-varying disturbances and a stronger capability to characterize the actual disturbance trends.

To avoid relying solely on qualitative judgments based on curve variations, this study further conducts a quantitative analysis of the trajectory-tracking errors, disturbance estimation errors, and control inputs for the different inner-loop control methods, as summarized in Table IV. Specifically, the root mean square error (RMSE) of the trajectory tracking is utilized to evaluate the tracking precision of the actual joint angles relative to the desired trajectories, and the RMSE of the disturbance estimation is employed to assess the observer's capability in estimating the system's total disturbance.

As evidenced by the results in Table IV, under fixed admittance conditions, the F-NLESO controller achieves a significant reduction in the average trajectory-tracking RMSE compared with the F-PID, decreasing from 0.032014 to 0.015899 rad, a reduction of approximately 50.34%. Similarly, the average disturbance estimation RMSE decreases from 0.842269 to 0.552851 Nm, representing a reduction of approximately 34.36%. These quantitative findings are consistent with the trends observed in the

Downloaded from https://www.cambridge.org/core. UNIVERSIDAD AUTONOMA METROPOLITANA, on 16 Nov 2026 at 03:23:03, subject to the Cambridge Core terms of use, available at https://www.cambridge.org/core/terms. https://doi.org/10.1017/S0263574726104056

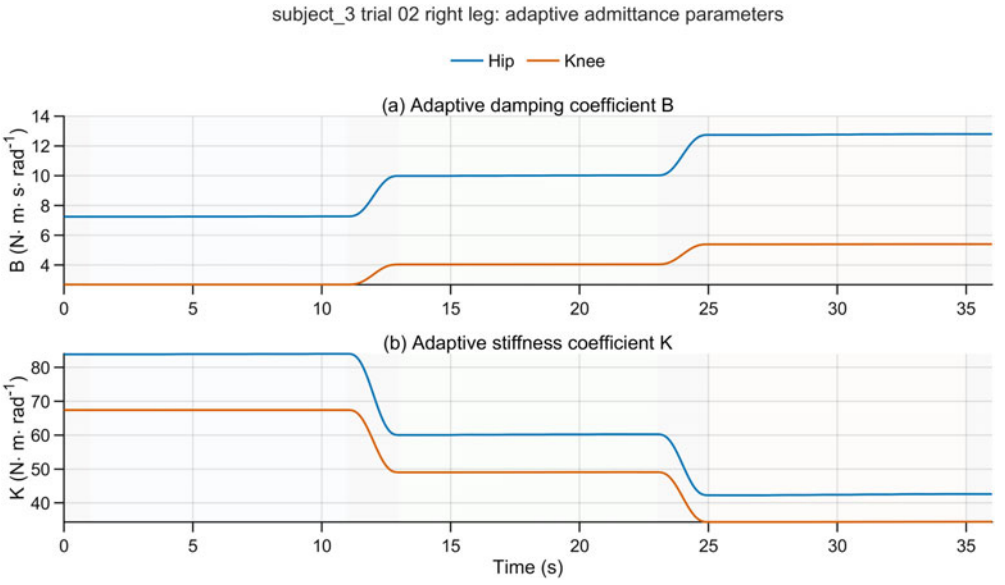


Figure 15. *Variation curves of the adaptive admittance parameters.*

trajectory tracking and disturbance estimation error plots, confirming that the PID controller suffers from larger errors during rapid joint variations and peak disturbances, whereas the NLESO-ADRC significantly enhances dynamic tracking performance through effective disturbance estimation and compensation.

Furthermore, compared with the F-LESO, the F-NLESO reduces the average trajectory-tracking RMSE by approximately 5.40% and the average disturbance estimation RMSE by approximately 13.69%. Under adaptive admittance conditions, the A-NLESO exhibits a reduction of approximately 5.39% in average trajectory-tracking RMSE and 13.66% in average disturbance estimation RMSE compared with the A-LESO. These results indicate that, regardless of whether a fixed or adaptive admittance outer loop is employed, the NLESO consistently outperforms the LESO in terms of both disturbance estimation precision and tracking stability.

6.3.2. Outer-loop performance comparison

In this section, the inner-loop controller is consistently configured as the NLESO-ADRC to isolate the effects of the outer-loop strategy. A comparative analysis is conducted between the fixed admittance control and the proposed adaptive admittance control, denoted as F-NLESO and A-NLESO, respectively, to evaluate the performance improvement offered by the adaptive mechanism.

As shown in the figure, the adaptive admittance parameters are not static throughout the motion but are adjusted segmentally according to the motion phase. For the hip joint, the damping coefficient B initially remains at approximately 7.3 Nms/rad, rises to about 10.0 Nms/rad between 11.5 and 13 s, and further increases to approximately 12.8 Nms/rad during the 23–25 s interval. Similarly, the damping coefficient B for the knee joint increases from an initial value of approximately 2.7 to 4.0 Nms/rad, eventually stabilizing at about 5.4 Nms/rad. Increasing the damping helps suppress potential oscillations during the reference correction process, thereby enhancing system response stability.

Corresponding to the increase in damping, the stiffness coefficient K exhibits an overall downward trend. The hip joint stiffness decreases from an initial value of approximately 83 Nms/rad to about 60 Nms/rad, eventually reaching 42 Nms/rad; meanwhile, the knee joint stiffness declines from approximately 67 to 49 Nms/rad, and finally stabilizes at about 34 Nms/rad. Reducing the stiffness helps decrease the rigid constraint imposed by the system on the reference trajectory, thereby ensuring that

Downloaded from https://www.cambridge.org/core. UNIVERSIDAD AUTONOMA METROPOLITANA, on 16 Nov 2026 at 03:23:03, subject to the Cambridge Core terms of use, available at https://www.cambridge.org/core/terms. https://doi.org/10.1017/S0263574726104056

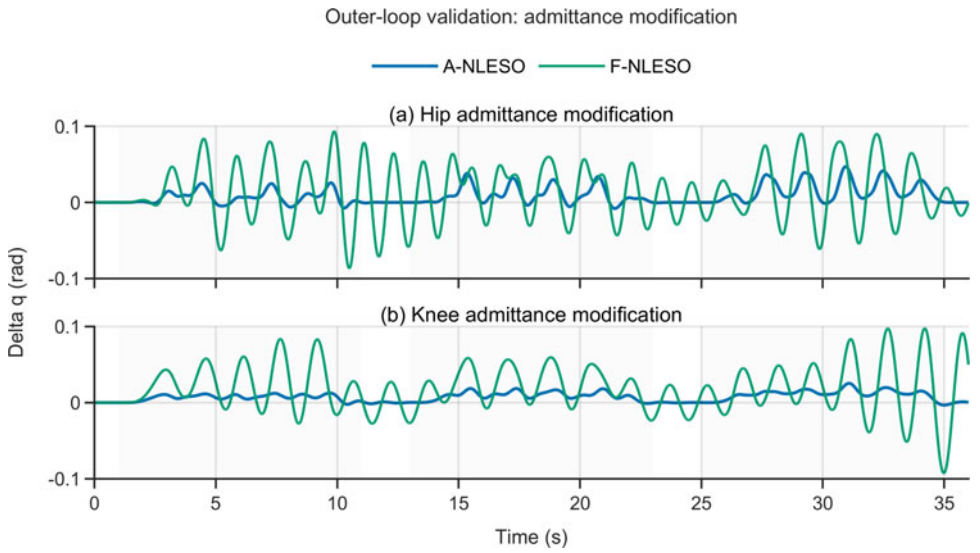


Figure 16. *Comparison of admittance correction amounts between fixed admittance and adaptive admittance control strategies.*

the reference correction during human–robot interaction is more compliant. The combination of these parameter adjustments achieves effective, compliant control of the system.

As illustrated in Figure 16, the fluctuations in the admittance correction amount for the F-NLESO are significantly more pronounced than those for the A-NLESO. For the hip joint, the F-NLESO exhibits large-amplitude oscillations during the 4–10, 15–21, and 27–34 s intervals, with peak values reaching approximately 0.08–0.10 rad. In contrast, the correction amount for the A-NLESO remains within the range of 0.03–0.04 rad, with a notable reduction in peak magnitude. Regarding the knee joint, the F-NLESO demonstrates significant fluctuations reaching ±0.1 rad during the 31–35 s interval. Conversely, the A-NLESO maintains its correction amount primarily within the 0–0.03 rad range, with a significantly reduced negative overshoot.

This figure further demonstrates that the fixed admittance strategy, due to its invariant parameters, struggles to adapt to the dynamic characteristics of different motion phases, leading to excessive reference corrections and distinct oscillations in the outer-loop corrected trajectory. By contrast, the adaptive admittance control, through real-time adjustment of damping and stiffness coefficients, ensures a smoother reference correction and effectively prevents over-correction by the outer loop.

Figures 17 and 18 show the joint angle tracking results and tracking errors for the A-NLESO and F-NLESO, respectively. As shown in Figure 17, with the NLESO-ADRC controller employed in the inner loop for both methods, both strategies achieve effective tracking of the desired hip and knee trajectories, demonstrating the robust tracking capability of the NLESO-ADRC inner loop.

Further comparison reveals that the F-NLESO exhibits noticeable local fluctuations at several peaks and transition stages, particularly near the 5–10 s and 27–33 s intervals for the hip joint, where the output curves display certain overshoots and oscillations. In contrast, the A-NLESO trajectory is smoother, successfully mitigating fluctuations caused by excessive local corrections while maintaining high tracking fidelity. For the knee joint, although both methods yield similar overall tracking performance, the A-NLESO exhibits slightly reduced oscillations at peak and transition positions.

Figures 18 shows that the tracking error curves for both methods are largely overlapping. Hip joint errors are primarily maintained within the 0.015–0.017 rad range, and knee joint errors are concentrated within 0–0.05 rad, with a peak value of approximately 0.055 rad. These results indicate that replacing the fixed admittance outer loop with an adaptive admittance strategy, while maintaining the same

Downloaded from https://www.cambridge.org/core. UNIVERSIDAD AUTONOMA METROPOLITANA, on 16 Nov 2026 at 03:23:03, subject to the Cambridge Core terms of use, available at https://www.cambridge.org/core/terms. https://doi.org/10.1017/S0263574726104056

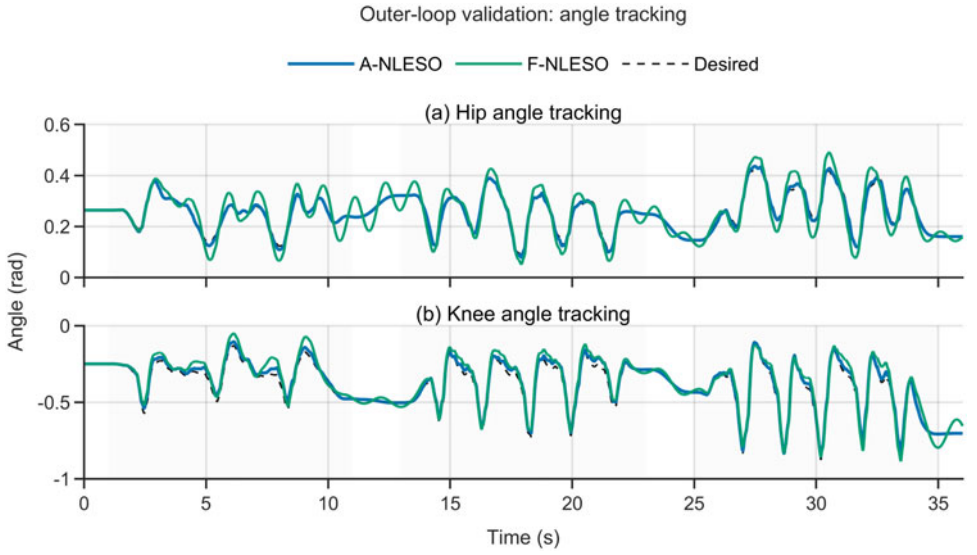


Figure 17. *Joint angle-tracking performance under fixed admittance and adaptive admittance control strategies.*

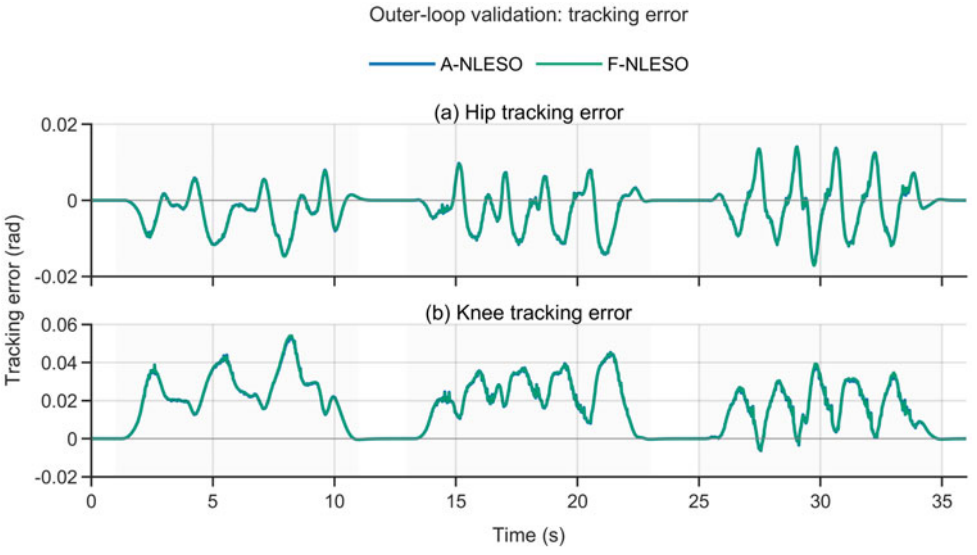


Figure 18. *Trajectory-tracking errors under fixed admittance and adaptive admittance control strategies.*

NLESO-ADRC inner loop, does not compromise trajectory-tracking precision and, more importantly, improves the local smoothness of the trajectory.

Figures 19 and 20 show the disturbance estimation results and estimation errors under fixed and adaptive admittance conditions, respectively. As shown in Figure 19, the actual disturbance exhibits distinct peaks across multiple motion stages. Both the A-NLESO and F-NLESO effectively track the trend of the actual disturbance and generate corresponding responses at the peaks. Although the estimation curves of both methods largely overlap, neither completely captures the sharp peaks of the actual disturbance.

Further analysis shown in Figure 20 reveals that the disturbance estimation error curves for both methods are nearly identical. For the hip joint, the disturbance estimation RMSE for A-NLESO and F-NLESO are 0.765757 and 0.767788 Nm, respectively, with noticeable error fluctuations appearing

Downloaded from https://www.cambridge.org/core. UNIVERSIDAD AUTONOMA METROPOLITANA, on 16 Nov 2026 at 03:23:03, subject to the Cambridge Core terms of use, available at https://www.cambridge.org/core/terms. https://doi.org/10.1017/S0263574726104056

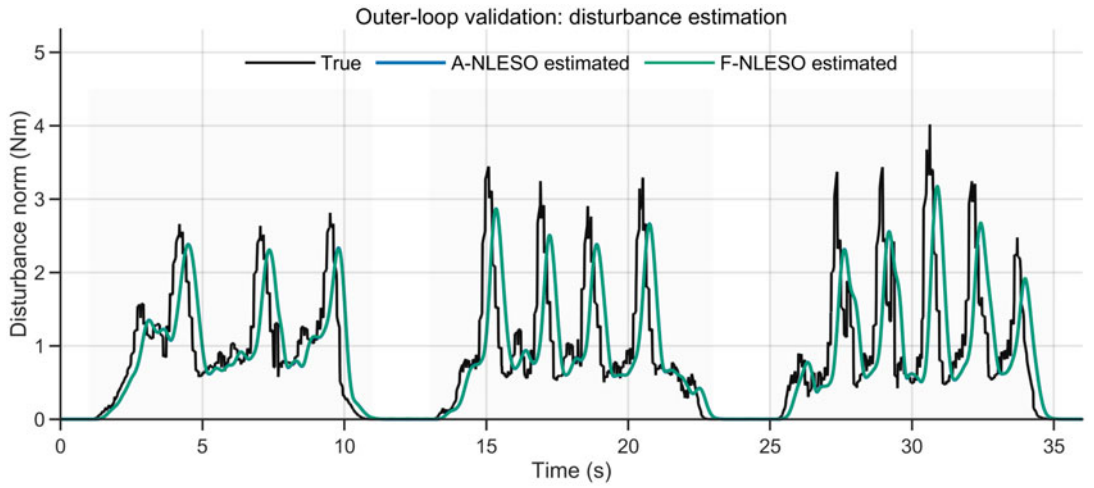


Figure 19. *Disturbance norm estimation under fixed admittance and adaptive admittance control strategies.*

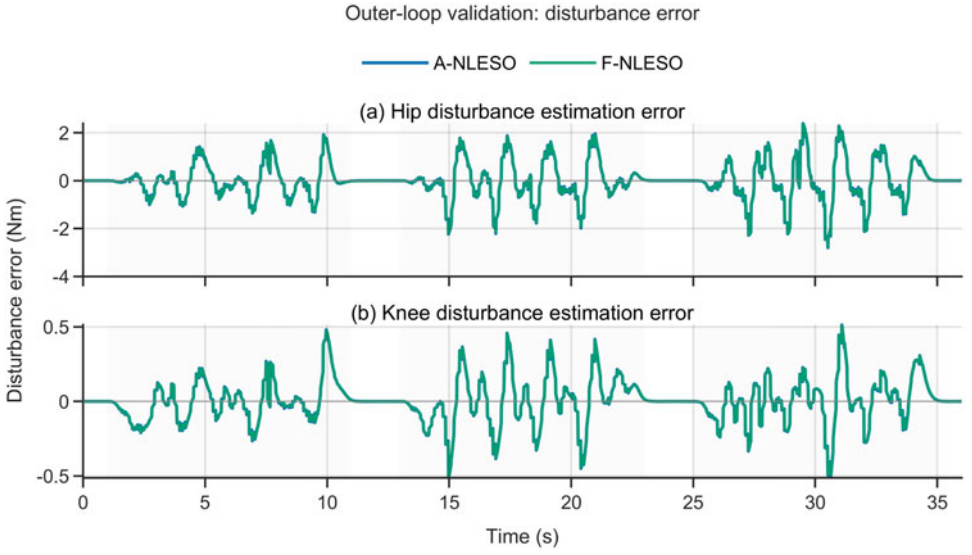


Figure 20. *Disturbance estimation error under fixed admittance and adaptive admittance control strategies.*

only during phases of rapid disturbance variation, such as 15–22 s and 27–34 s. For the knee joint, the error magnitudes are generally small, primarily concentrated within the range of ±0.5 Nm, with RMSE values of 0.147419 and 0.147615 Nm, respectively – a difference of approximately 0.13%. These results indicate that the disturbance estimation precision for both hip and knee joints is consistent under both outer-loop strategies.

In summary, the performance difference in disturbance estimation between A-NLESO and F-NLESO is negligible, confirming that the system's disturbance estimation and anti-disturbance compensation capabilities are primarily determined by the NLESO-ADRC inner loop. The primary role of the adaptive admittance outer loop is not to further enhance disturbance estimation accuracy, but rather to improve the stability and compliance of the reference trajectory correction process, while maintaining the consistent disturbance estimation performance of the inner loop.

Downloaded from https://www.cambridge.org/core. UNIVERSIDAD AUTONOMA METROPOLITANA, on 16 Nov 2026 at 03:23:03, subject to the Cambridge Core terms of use, available at https://www.cambridge.org/core/terms. https://doi.org/10.1017/S0263574726104056

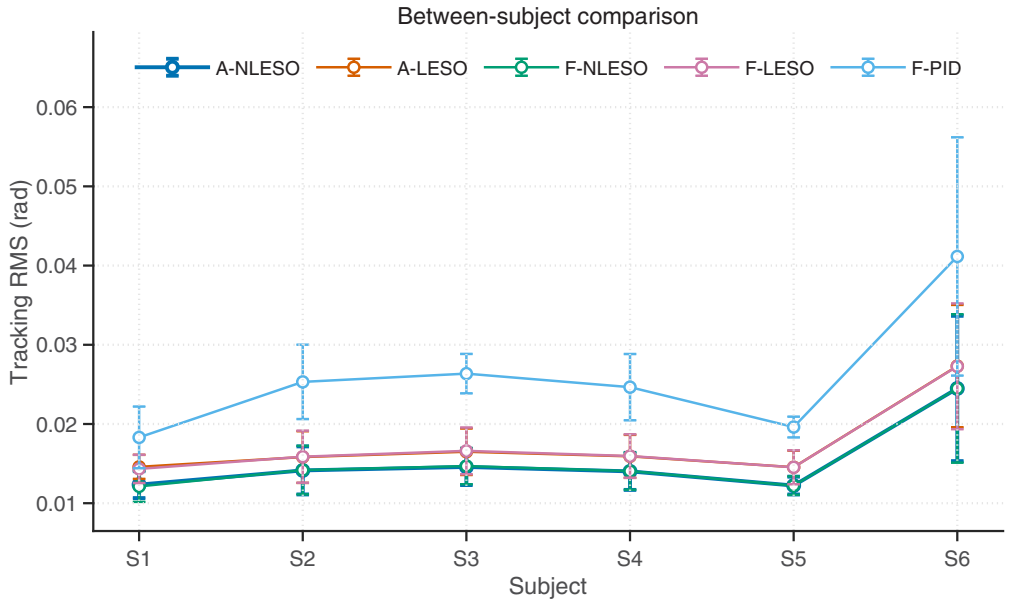


Figure 21. *Comparison of trajectory-tracking RMSEs across different subjects.*

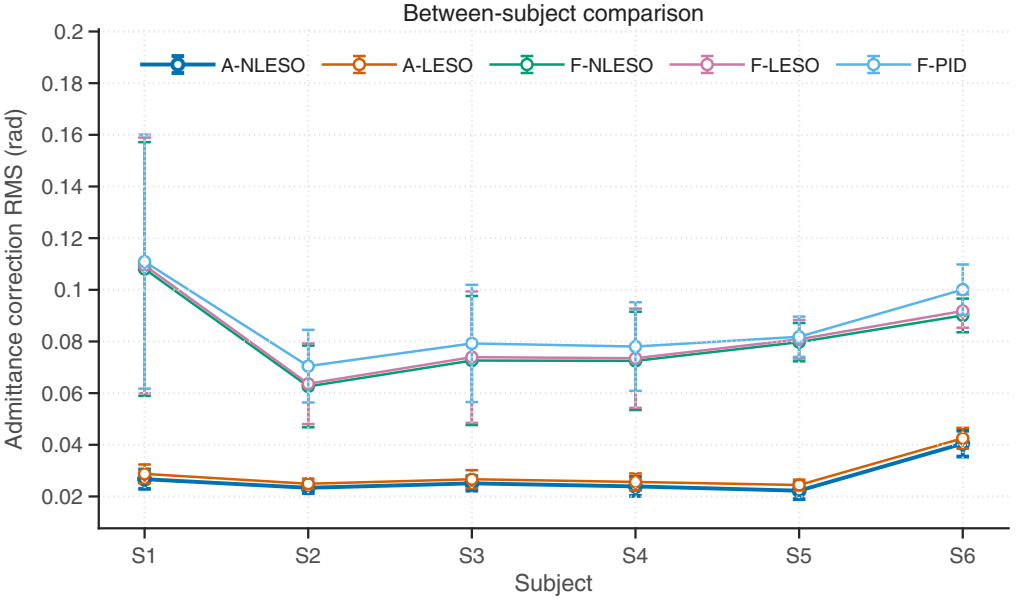


Figure 22. *Comparison of admittance correction RMS values across different subjects.*

6.3.3. Consistency verification across multiple experiments

To demonstrate the robustness and generalizability of the proposed control strategy, this section extends the analysis from the typical experimental trial (Subject 3) to a comprehensive cohort of all participants. A comparative analysis is performed across all experimental datasets to validate the consistency and reliability of the NLESO-ADRC-based adaptive admittance control method under varying individual gait characteristics and human–robot interaction patterns.

Figures 21–23 compare the performance of different control methods across multiple experimental trials in terms of trajectory-tracking accuracy, admittance correction magnitude, and disturbance

Downloaded from https://www.cambridge.org/core. UNIVERSIDAD AUTONOMA METROPOLITANA, on 16 Nov 2026 at 03:23:03, subject to the Cambridge Core terms of use, available at https://www.cambridge.org/core/terms. https://doi.org/10.1017/S0263574726104056

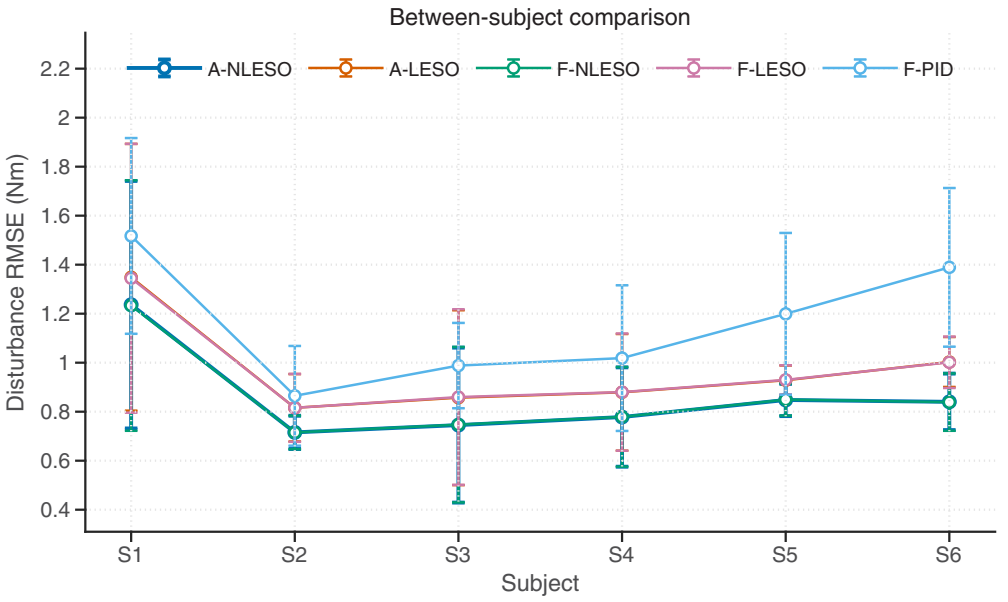


Figure 23. *Comparison of disturbance estimation RMSE across different subjects.*

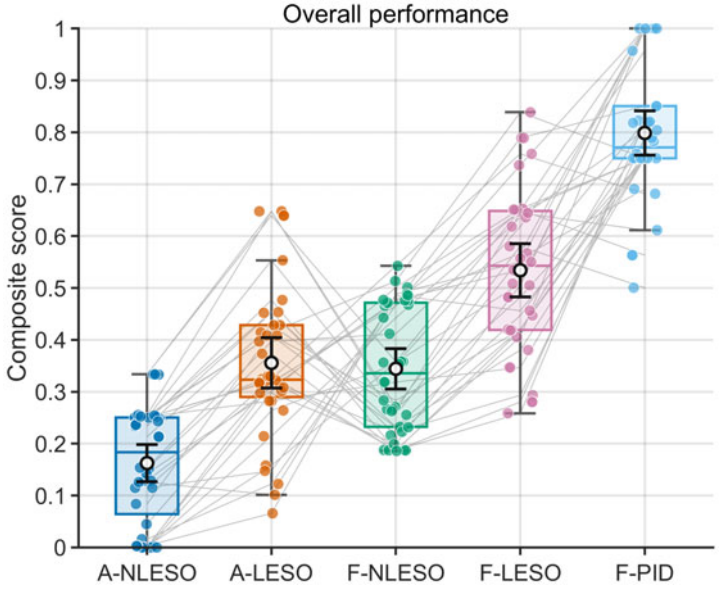


Figure 24. *Comparison of comprehensive performance scores across different subjects.*

estimation precision. Overall, the F-PID controller exhibits inferior performance in most trials, characterized by higher trajectory-tracking RMS and disturbance estimation RMSE, which indicates that the traditional PID inner loop has limited dynamic tracking and disturbance adaptation capabilities under varying experimental inputs. Although the F-LESO offers improvements over the F-PID, its overall performance remains inferior to the NLESO-based methods.

In contrast, both the A-NLESO and F-NLESO maintain low levels of tracking error and disturbance estimation RMSE, demonstrating that the NLESO-ADRC inner loop consistently enhances trajectory tracking and disturbance estimation capabilities across diverse experimental conditions. Furthermore, the minimal difference between A-NLESO and F-NLESO in these metrics suggests that the adaptive admittance outer loop does not compromise the inherent tracking and disturbance rejection performance

Downloaded from https://www.cambridge.org/core. UNIVERSIDAD AUTONOMA METROPOLITANA, on 16 Nov 2026 at 03:23:03, subject to the Cambridge Core terms of use, available at https://www.cambridge.org/core/terms. https://doi.org/10.1017/S0263574726104056

Table V. *Performance improvement rates of A-NLESO compared with baseline methods.*

Comparison methods	Tracking RMS reduction	Admittance correction reduction	Disturbance RMSE reduction
A-NLESO versus F-PID	50.65%	59.19%	34.53%
A-NLESO versus F-LESO	5.99%	49.91%	13.92%
A-NLESO versus F-NLESO	0.62%	49.00%	0.26%
A-NLESO versus A-LESO	5.39%	3.33%	13.66%

of the NLESO-ADRC inner loop. Regarding the admittance correction RMS, both the A-NLESO and A-LESO significantly outperform fixed admittance methods, indicating that the adaptive admittance outer loop effectively reduces the amplitude of reference trajectory correction, thereby improving the stability and compliance of the outer-loop regulation process.

To comprehensively evaluate the performance of different control methods, Figure 24 presents the distribution of comprehensive performance scores. The results show that the A-NLESO consistently achieves the lowest scores, with the majority of samples concentrated in the lower range, whereas the F-PID yields the highest scores, indicating the weakest comprehensive control performance. The A-LESO and F-NLESO fall into the intermediate range, with the F-LESO scoring higher overall than the former two. The gray lines connecting the same experimental samples under different control methods reveal a downward trend in scores from F-PID to A-NLESO, demonstrating that the proposed method consistently yields lower comprehensive penalty scores across the majority of experimental samples.

Combined with the results in Figures 21–24, it can be concluded that the adaptive admittance outer loop primarily improves the stability and compliance of reference trajectory correction, although the NLESO-ADRC inner loop focuses on enhancing trajectory tracking and disturbance estimation performance. Their integration enables superior comprehensive control performance across diverse experimental conditions.

6.3.4. Discussion and analysis

The experimental results presented in the previous sections confirm that the A-NLESO method consistently achieves superior comprehensive control performance across both typical and multiple experimental datasets. To further quantify the sources of this performance enhancement, Table V provides the key performance improvement rates of the A-NLESO method compared with various baseline controllers. Unlike the comprehensive performance metrics discussed previously, Table V focuses on the relative contributions of the adaptive admittance outer loop and the NLESO-ADRC inner loop to the overall system performance improvement.

As shown in Table V, compared with the F-PID controller, the A-NLESO method achieves reductions of approximately 50.65%, 59.19%, and 34.53% in average tracking RMSE, average admittance correction RMS, and average disturbance estimation RMSE, respectively, demonstrating that the proposed method has significant comprehensive performance advantages over the conventional PID-based control scheme. In comparison with the F-NLESO, the average admittance correction RMS of the A-NLESO is reduced by approximately 49.00%, whereas the average tracking RMSE and average disturbance estimation RMSE are reduced by only approximately 0.62% and 0.26%, respectively. This indicates that the primary function of the adaptive admittance outer loop is to minimize the magnitude of reference trajectory corrections and enhance the stability of the outer-loop regulation, rather than directly augmenting the tracking or disturbance estimation capabilities of the inner loop. Compared with the A-LESO, the average disturbance estimation RMSE of the A-NLESO is reduced by approximately 13.66%, confirming that the NLESO-ADRC inner loop possesses superior disturbance estimation capability under the same adaptive admittance outer-loop configuration.

In summary, the performance enhancement of the A-NLESO originates from the synergistic interaction between the inner and outer loops: the NLESO-ADRC inner loop primarily improves

Downloaded from https://www.cambridge.org/core. UNIVERSIDAD AUTONOMA METROPOLITANA, on 16 Nov 2026 at 03:23:03, subject to the Cambridge Core terms of use, available at https://www.cambridge.org/core/terms. https://doi.org/10.1017/S0263574726104056

trajectory-tracking precision and disturbance estimation, whereas the adaptive admittance outer loop primarily reduces the admittance correction magnitude and improves the smoothness of reference trajectory modification. Their integration enables the system to maintain high tracking fidelity and anti-disturbance performance while concurrently achieving compliant outer-loop regulation. Multitrial experimental results further demonstrate that the A-NLESO consistently maintains low comprehensive penalty scores across all subject trials (S1–S6), confirming the cross-trial adaptability and control stability of the proposed method.

7. Conclusion

To address the challenge of simultaneously achieving high trajectory-tracking accuracy, compliant regulation, and robust disturbance rejection in human–robot interaction systems, this paper proposes a dual-loop control architecture that integrates an adaptive admittance outer loop with an NLESO-ADRC inner loop. This approach employs adaptive admittance control to perform compliant modifications on the reference trajectory, although the NLESO-ADRC inner loop estimates and compensates for total system disturbances. Consequently, this enhances the system's trajectory-tracking precision, compliance, and anti-disturbance stability across diverse movement states.

Simulation and experimental results demonstrate that the NLESO-ADRC inner loop outperforms conventional PID and LESO controllers in terms of trajectory tracking and disturbance estimation, effectively reducing joint-tracking errors and enhancing disturbance rejection. The outer-loop comparison indicates that adaptive admittance successfully mitigates the excessive corrections observed under fixed admittance, resulting in a smoother and more rational reference trajectory modification process without compromising the inner loop's inherent tracking and estimation performance. Comprehensive performance evaluations across multiple trials further confirm that the proposed adaptive admittance plus NLESO-ADRC method exhibits superior performance in trajectory tracking, admittance correction, and disturbance estimation, validating the effectiveness and cross-trial adaptability of the approach.

It should be pointed out that although this article uses motion data collected from actual exoskeleton-wearing experiments as input for the control system, which can more realistically reflect the motion characteristics under different walking states compared with idealized simulation trajectories, the current verification still mainly adopts offline/semi physical methods and has not yet completed complete real-time closed-loop human–machine interaction control on actual exoskeleton platforms. Therefore, the real-time computing performance, interactive safety, and stability of the control algorithm under real human–machine coupling conditions still need further verification when facing complex disturbances and abnormal working conditions. In addition, the current double-layer adaptive admittance parameters are mainly adjusted based on walking speed and human–computer interaction status and have not yet introduced information such as electromyographic signals and plantar pressure that can further reflect human motion intention and gait stages; at present, the validation has not yet involved patients with lower-limb motor dysfunction such as stroke and spinal cord injury, and its clinical applicability still needs further research.

In response to the above limitations, future research will be conducted from the following aspects. First, the real-time deployment of the proposed dual loop control algorithm will be implemented on the existing second-generation lightweight exoskeleton experimental platform, and closed-loop walking experiments will be conducted under real human–machine coupling conditions to further verify the real-time performance, stability, and human–machine interaction performance of the controller. Second, multimodal human body information such as electromyographic signals, plantar pressure, and joint motion information are introduced to study the gait stage recognition and switching mechanism driven by physiological signals, and further combined with double-layer adaptive admittance parameter adjustment to improve the real-time adaptability of the control system to human motion intention and gait changes. Finally, based on the completion of real-time closed-loop experiments on healthy subjects, clinical trials will be gradually conducted for patients with stroke, spinal cord injury, and other lower-limb

Downloaded from https://www.cambridge.org/core. UNIVERSIDAD AUTONOMA METROPOLITANA, on 16 Nov 2026 at 03:23:03, subject to the Cambridge Core terms of use, available at https://www.cambridge.org/core/terms. https://doi.org/10.1017/S0263574726104056

motor dysfunction to evaluate the applicability of the proposed method under individual differences, abnormal gait, and different rehabilitation stages. Finally, a Hardware in the Loop (HIL) safety testing environment will be constructed to evaluate the stability and safety of the controller under abnormal conditions such as sensor noise and faults, communication delays, actuator constraints, and sudden external disturbances. This will provide further experimental evidence for the long-term operation and clinical application of the actual exoskeleton in the future.

Author contributions. **Di Zhang**, **Yiming Liu,** and **Liuyi Ling** conceived and designed the study. **Yiming Liu** was responsible for the design and development of the rehabilitation training robot, **Di Zhang** conducted the experiments and performed data gathering. **Liuyi Ling** supervised the project, provided resources, and performed the final revision of the article. All the authors have read and approved the final manuscript.

Financial support. This work was supported by the Research and Development Fund of the Institute of Environmental Friendly Materials and Occupational Health, Anhui University of Science and Technology [grant number: ALW2022YF06]; the Academic Support Project for Top-notch Talents in Disciplines (Majors) of Colleges and Universities in Anhui Province, China [grant number: gxbjZD2021052]; and the University Synergy Innovation Program of Anhui Province, China [grant number: GXXT-2022-053].

Competing interests. The authors declare that no conflicts of interest exist.

Ethical approval. This study involves human subjects. All ethical and experimental procedures and protocols have been reviewed and approved by the Biomedical Research Ethics Committee of Anhui University of Science and Technology, with ethical review approval number 2023-5. All experimental operations were conducted in strict compliance with relevant ethical guidelines and regulations.

References

[1] Q. Wu, Z. Wang and Y. Chen, "SEMG-based adaptive cooperative multi-mode control of a soft elbow exoskeleton using neural network compensation," *IEEE Trans. Neural Syst. Rehabil. Eng.* **31**, 3384–3396 (2023).
[2] Y. Ma, X. Wu, J. Yi, C. Wang and C. Chen, "A review on human-exoskeleton coordination towards lower limb robotic exoskeleton systems," *Int. J. Robot. Autom.* **34**(4), 431–451 (2019).
[3] W. Cao, C. Chen, D. Wang, X. Wu, L. Chen, T. Xu and J. Liu, "A lower limb exoskeleton with rigid and soft structure for loaded walking assistance," *IEEE Robot. Autom. Lett.* **7**(1), 454–461 (2022).
[4] J. Cao, J. Zhang, C. Wang, K. Li, J. Zhang, G. Wang and H. Ren, "Variable admittance control of high compatibility exoskeleton based on human–robotic interaction force," *Chin. J. Mech. Eng.* **37**(1), 119 (2024).
[5] G. Masengo, X. Zhang, R. Dong, A. B. Alhassan, K. Hamza and E. Mudaheranwa, "Lower limb exoskeleton robot and its cooperative control: A review, trends, and challenges for future research," *Front. Neurorobotics* **16**, 913748 (2023).
[6] E. B. Küçüktabak, Y. Wen, S. J. Kim, M. R. Short, D. Ludvig, L. Hargrove, E. J. Perreault, K. M. Lynch and J. L. Pons, "Haptic transparency and interaction force control for a lower limb exoskeleton," *IEEE Trans. Robot.* **40**, 1842–1859 (2024).
[7] X. Gao, P. Zhang, X. Peng, J. Zhao, K. Liu, M. Miao, P. Zhao, D. Luo and Y. Li, "Autonomous motion and control of lower limb exoskeleton rehabilitation robot," *Front. Bioeng. Biotechnol.* **11**, 1223831 (2023).
[8] Y. M. Hamad, Y. Aydin and C. Basdogan, "Adaptive human force scaling via admittance control for physical human–robot interaction," *IEEE Trans. Haptics* **14**(4), 750–761 (2021).
[9] C. Li, H. Di, Y. Liu and K. Liu, "Research on lower limb exoskeleton trajectory tracking control based on the dung beetle optimizer and feedforward proportional-integral-derivative controller," *Actuators* **13**(9), 3442 (2024).
[10] U. Hanifah, A. Adinda, A. Rahmatillah, I. Sapuan, K. Ain, H. Septanto and R. Chai, "Online PID-neural network for tracking lower limb rehabilitation exoskeleton angular position," *Bull. Electr. Eng. Inform.* **14**(5), 3371–3380 (2025).
[11] S. K. Hasan, "A realistic model reference computed torque control strategy for human lower limb exoskeletons," *Actuators* **13**(11), 445 (2024). MDPI.
[12] Y. Han, H. Ma, Y. Wang, D. Shi, Y. Feng, X. Li, Y. Shi, X. Ding and W. Zhang, "Neural network robust control based on computed torque for lower limb exoskeleton," *Chin. J. Mech. Eng.* **37**(1), 37 (2024).
[13] Y. Shi, J. Kou, Z. Chen, Y. Wang and Q. Guo, "Model parameters identification and backstepping control of lower limb exoskeleton based on enhanced Whale algorithm," *Chin. J. Mech. Eng.* **37**(1), 26 (2024).
[14] G.-W. Zhang, P. Yang, J. Wang, J.-J. Sun and Y. Zhang, "Integrated observer-based fixed-time control with backstepping method for exoskeleton robot," *Int. J. Autom. Comput.* **17**(1), 71–82 (2020).
[15] K. Thakkar, V. Paredes and A. Hereid, "Adaptive feedback regulator for powered lower-limb exoskeleton under model uncertainty," arXiv preprint arXiv:2104.11775 (2021).
[16] Y. Zhou, Z. Sun, B. Chen, G. Huang, X. Wu and T. Wang, "Human gait tracking for rehabilitation exoskeleton: Adaptive fractional order sliding mode control approach," *Intell. Robot.* **3**(1), 95112 (2023).

Downloaded from https://www.cambridge.org/core. UNIVERSIDAD AUTONOMA METROPOLITANA, on 16 Nov 2026 at 03:23:03, subject to the Cambridge Core terms of use, available at https://www.cambridge.org/core/terms. https://doi.org/10.1017/S0263574726104056

[17] R. Pérez-San Lázaro, I. Salgado and I. Chairez, "Adaptive sliding-mode controller of a lower limb mobile exoskeleton for active rehabilitation," *ISA Trans.* **109**, 218–228 (2021).
[18] S. Aole, I. Elamvazuthi, L. Waghmare, B. Patre and F. Meriaudeau, "Improved active disturbance rejection control for trajectory tracking control of lower limb robotic rehabilitation exoskeleton," *Sensors* **20**(13), 3681 (2020).
[19] J. Han, "From PID to active disturbance rejection control," *IEEE Trans. Ind. Electron.* **56**(3), 900–906 (2009).
[20] J. Michalski, M. Mrotek, M. Retinger and P. Kozierski, "Adaptive active disturbance rejection control with recursive parameter identification," *Electronics* **13**(16), 3114 (2024).
[21] Q.-T. Dao, V.-V. Dinh, M.-C. Trinh, V.-C. Tran, V.-L. Nguyen, M.-D. Duong and N.-T. Bui, "Nonlinear extended observer-based ADRC for a lower-limb PAM-based exoskeleton," *Actuators* **11**(12), 369 (2022). MDPI.
[22] Z. Gao, "Active Disturbance Rejection Control: A Paradigm Shift in Feedback Control System Design," **In:** *2006 American Control Conference* (IEEE, 2006) p. 7.
[23] Y. Long, Z. Du, L. Cong, W. Wang, Z. Zhang and W. Dong, "Active disturbance rejection control based human gait tracking for lower extremity rehabilitation exoskeleton," *ISA Trans.* **67**, 389–397 (2017).
[24] A. T.-E. Benyahia, M. Stanković, R. Madonski, O. Babayomi and S. M. Manojlović, "Improving control performance by cascading observers: Case of ADRC with cascade ESO," *IEEE/CAA J. Autom. Sinica* **12**(8), 1702–1712 (2024).
[25] Z. Yan, S. Deng, Z. Yang, X. Zhao, N. Yang and Y. Lu, "Improved nonlinear active disturbance rejection control for a continuous-wave pulse generator with cascaded extended state observer," *Control Eng. Pract.* **146**, 105897 (2024).
[26] J. Michalski, Młaj Mrotek, D. Pazderski, P. Kozierski and M. Retinger, "Improving performance of ADRC control systems affected by measurement noise using Kalman filter-tuned extended state observer," *Electronics* **13**(24), 4916 (2024).
[27] K. He, C. Dong and Q. Wang, "Active disturbance rejection control for uncertain nonlinear systems with sporadic measurements," *IEEE/CAA J. Autom. Sinica* **9**(5), 893–906 (2022).
[28] M. Ali and H. Mirinejad, "Robust tracking control of flexible manipulators using hybrid backstepping/nonlinear reduced-order active disturbance rejection control," *ISA Trans.* **149**, 229–236 (2024).
[29] M. Mrotek and J. Michalski, "Trajectory Tracking with Generalized Active Disturbance Rejection Control Using Kalman Filter-based Extended State Observer," **In:** *28th International Conference on Methods and Models in Automation and Robotics (MMAR)* (IEEE, 2024) pp. 316–321.
[30] D. Centeno-Barreda, S. Salazar-Cruz, R. López-Gutiérrez, Y. Rosales-Luengas and R. Lozano, "Lower limb exoskeleton for gait rehabilitation with adaptive nonsingular sliding mode control," *Robotica* **42**(11), 3819–3838 (2024).
[31] A. M. Dollar and H. Herr, "Lower extremity exoskeletons and active orthoses: Challenges and state-of-the-art," *IEEE Trans. Robot.* **24**(1), 144–158 (2008).
[32] N. Hogan, "Impedance Control: An Approach to Manipulation," **In:** *1984 American Control Conference* (IEEE, 1984) pp. 304–313.
[33] A. Q. L. Keemink, H. Van der Kooij and A. H. A. Stienen, "Admittance control for physical human–robot interaction," *Int. J. Robot. Res.* **37**(11), 1421–1444 (2018).
[34] J. Kou, Y. Wang, Z. Chen, Y. Shi and Q. Guo, "Gait planning and multimodal human-exoskeleton cooperative control based on central pattern generator," *IEEE/ASME Trans. Mechatronics* **30**(4), 2598–2608 (2025).
[35] J. G. Kou, Y. X. Wang, Z. L. Chen, Y. Shi, Q. Guo and M. Xu, "Flexible assistance strategy of lower limb rehabilitation exoskeleton based on admittance model," *Sci. China Technol. Sci.* **67**(3), 823–834 (2024).
[36] C. Gao, C. Wang, H. Li, J. Zhang, X. Du and J. Zhang, "Human–machine coupling dynamics modeling and adaptive admittance control of lower limb rehabilitation robot," *Robotica* **43**(10), 3419–3441 (2025).
[37] H. Zhan, J. Kou, Y. Cao, W. Wang, J. Zhang, Y. Shi and Q. Guo, "Model identification and admittance control with neighborhood field optimization in human–exoskeleton cooperative motion," *Robotica* **43**(12), 4560–4575 (2025).
[38] T. Li, H. Xing, E. Hashemi, H. D. Taghirad and M. Tavakoli, "A brief survey of observers for disturbance estimation and compensation," *Robotica* **41**(12), 3818–3845 (2023).
[39] Z. Chen, Q. Guo, T. Li, Y. Yan and D. Jiang, "Gait prediction and variable admittance control for lower limb exoskeleton with measurement delay and extended-state-observer," *IEEE Trans. Neural Netw. Learn. Syst.* **34**(11), 8693–8706 (2023).
[40] J. Kou, Z. Yang, Z. Chen, Y. Wang, Y. Shi and Q. Guo, "Active–passive switching admittance control for lower limb exoskeleton with nonlinear disturbance observer," *Sens. Actuators A: Phys.* **398**, 117250 (2026).
[41] M. Elstohy and K.-W. Gwak, "Nonlinear disturbance observer-based PID sliding mode admittance control of a lower-limb wearable robot considering a human–exoskeleton coupling dynamics in a swing phase," *Int. J. Dyn. Control* **14** (3), 98 (2026).

Cite this article: D. Zhang, L. Ling and Y. Liu, "Dual-loop control of lower-limb exoskeletons using adaptive admittance and nonlinear extended state observer-based active disturbance rejection", Robotica. https://doi.org/10.1017/S0263574726104056

Downloaded from https://www.cambridge.org/core. UNIVERSIDAD AUTONOMA METROPOLITANA, on 16 Nov 2026 at 03:23:03, subject to the Cambridge Core terms of use, available at https://www.cambridge.org/core/terms. https://doi.org/10.1017/S0263574726104056